이학박사 학위논문

Fabrication and Characterization of Vertically Aligned Graphene Gaps at THz Regime

수직으로 정렬된 그래핀 갭의 제작과 테라헤르츠파 영역에서의 특성

2020 년 8 월

서울대학교 대학원

물리천문학부 물리학 전공

김 성 환

Fabrication and Characterization of Vertically Aligned Graphene Gaps at THz Regime

지도 교수 홍 성 철

이 논문을 이학박사 학위논문으로 제출함
2020 년 7 월

서울대학교 대학원
물리천문학부 물리학 전공
김 성 환

김성환의 이학박사 학위논문을 인준함
2020 년 6 월

위 원 장 _____ 차 국 린 _____ (인)

부위원장 _____ 홍 성 철 _____ (인)

위 원 _____ 박 건 식 _____ (인)

위 원 _____ 전 헌 수 _____ (인)

위 원 _____ 박 영 미 _____ (인)

Abstract

In this work, a vertically aligned graphene gap array composed of a copper-graphene-copper structure was investigated for optical measurements at terahertz regime. The graphene gap array was manufactured by directly synthesizing graphene on the first patterned copper thin film followed by depositing the second copper layer. Structural features of the graphene between the copper thin films were characterized by Cs-corrected transmission electron microscope and resonant Raman spectroscopy. The results revealed that the number of layers and the crystallinity of graphene on the copper surface can be controlled by adjusting the synthesis temperature and pre-annealing time in plasma enhanced chemical vapor deposition process. And the gap size can be defined by a multiple of van der Waals distance according to the number of graphene layers. Furthermore, the optical properties of a graphene gap slit array at terahertz regime was investigated by terahertz-time domain spectroscopy. Even though the gap size is a sub-nanometer for single-layer graphene gap, the terahertz transmitted amplitude revealed that the fabricated graphene gap slit array is fully functional. The constant normalized terahertz amplitude through the graphene gap slit array in the frequency domain was explained by the graphene

treated as a gap material with a complex dielectric constant using analysis of the capacitor model. The results in this work can open a new route for the fabrication techniques and characterization of structural and optical properties in many optical, electronic and optoelectronic applications using two-dimensional materials such as hexagonal boron nitride (h-BN), molybdenum disulfide (MoS_2), and etc.

Keywords : nanogap, graphene, Atomic layer lithography, Raman spectroscopy, THz-time domain spectroscopy

Student Number : 2013-30918

Table of Contents

List of Figures

Chapter 1. Introduction

1.1 Extraordinary optical transmission

Light is usually transmitted through the hole, when a metal thin film with a hole is illuminated. The transmission of light typically decreases as the hole size decreases. However, extraordinary optical transmission occurs at some particular frequencies when light is incident to a metal thin film with a subwavelength hole array [1]. The extraordinary optical transmission in visible and near infrared is explained by the excitation of surface plasmon in the metal thin film [2, 3]. The surface plasmon which is collective oscillations of free electrons in a metal thin film is excited by the visible and near infrared at the interface between the metal and the insulating layer [4]. Since the discovery of extraordinary optical transmission through the subwavelength hole array, the study of fundamental optical phenomena in subwavelength region has been rapidly developed for two decades [5, 6].

Based on the previous results, a subwavelength gap in a metal thin film should be prepared with nanometer scale features for extraordinary optical transmission in wavelengths located at visible and infrared ranging from hundreds of nanometers to tens of micrometers. Similarly, Considering the gap-to-wavelength ratio, a

micrometer-sized gap was applied to extraordinary optical transmission in terahertz (THz) waves with wavelengths ranging from hundreds of micrometers to several millimeters [7, 8]. Interestingly, even though the gap size was reduced to a nanometer scale, extraordinary optical transmission was still observed in the THz waves [9]. As a result, a nanogap whose gap size is on the nanometer scale can be fully functional for extraordinary optical transmission in broad wavelengths including visible, infrared, and THz waves.

1.2 Field enhancement in a nanogap at THz regime

THz wave is located between the infrared and microwave so that its frequency is much lower than the plasma frequency of a metal [10]. Thus, the surface plasmon which contribute to extraordinary optical transmission for a nanogap array is hardly excited on the metal thin film by THz waves. Instead, the capacitor model was adopted to explain it for a nanogap array in THz waves [11]. According to the capacitor model, when a nanogap is normally illuminated by THz wave with an electric field polarized perpendicular to the nanogap, a current is induced in a metal thin film. Then, charges are accumulated at the edges of the metal thin film, like a capacitor. Eventually, the nanogap acts as an antenna, resulting in the THz transmission.

Interestingly, an electric field inside the nanogap is formed by the accumulated charges during the THz transmission. In addition, its intensity largely increases as a decrease in the nanogap size [12]. Hence, field enhancement defined by the intensity ratio of the electric field formed inside the nanogap to the incident electric field is strongly dependent on the gap size. A previous demonstration was reported that as a gap size decreases, the field enhancement at a resonant frequency hugely increases up to 8,000 [13]. As a result, a very large electric field can be obtained inside a nanogap, which can

be utilized for many applications such as molecular sensing, surface enhanced Raman spectroscopy (SERS), nonlinear optics, field emission, memory devices, and so on. For example, small amounts of molecules inside a nanogap with high field enhancement are effectively detected compared to a conventional detection requiring a very large amount of molecules [14]. And undetectable signals by low intensities in Raman spectroscopy are greatly amplified due to the high field enhancement using a nanogap [15]. Consequently, for nanogap-based applications, nanogap with a very narrow gap size should be required to achieve high field enhancement.

1.3 Sub-nanometer gap using graphene

In order to increase field enhancement, the nanogap size should be smaller and smaller. With the development of nanotechnology, manufacturing methods have been diversified and the size of a nanogap has greatly reduced to a few nanometers, or less than 1 nm [16-21]. Especially, for a sub-nanometer gap, graphene can be used as a gap spacer [22-27]. Graphene is an allotrope of carbon with a two-dimensional honeycomb lattice [28]. Thus, graphene between metal thin films plays a role as an atomically thin spacer to separate them at a sub-nanometer distance. It is the fact that a interlayer distance for a multi-layer graphene is the van der Waals distance [29]. When a multi-layer graphene is applied as a gap spacer, the gap size is determined by a multiple of the van der Waals distance according to the number of graphene layers. For a gap composed of graphene as a gap material, it is called a graphene gap to distinguish it from other nanogap.

In most cases, a graphene gap is obtained by transferring graphene on a desired metal film [26, 27]. However, there are some issues causing low gap performances. First of all, graphene is inevitably damaged and contaminated during the transfer process [30, 31]. Second, a graphene gap is locally formed on a metal film compared to the transferred graphene area, limiting patterning gap

structure in large area. Third, a graphene gap is horizontal to the substrate, resulting in a weak light confinement and a poor signal-to-noise ratio for normal incidence. In addition, it is hard to directly quantify field enhancement inside the graphene gap. From these reasons, a transfer-free route for a desired graphene gap structures with large area pattern is prerequisite for nanogap-based applications.

Chapter 2. Preparation of graphene gap array

A nanogap array with a small gap size and a large area pattern in wafer-scale can be effectively applicated in many optical and optoelectronic devices, such as modulators, sensors, filters, and so on [32-37]. In this chapter, the fabrication of a graphene gap array will be discussed in detail, following the fabrication process of a nanogap array.

2.1 Atomic layer lithography for nanogap fabrication

In general, microstructure with various patterns is realized by nanotechnology techniques, such as lithography, deposition, etching, and etc. [38-40]. Especially, focused ion beam (FIB) milling and electron-beam lithography are widely employed to pattern a metal film with a nanogap [17, 21]. However, two methods are a time-consuming process for patterning in large area because the working area is very small compared to the whole sample area. Also, the size of a nanogap is limited to hundreds of nm due to the beam size [41].

In order to solve this issues, atomic layer lithography was developed as a new approach using photolithography and atomic layer deposition (ALD) [42, 43]. In atomic layer lithography, a nanogap array can be patterned with various shapes by photolithography in a

large area. And ALD can deposit an insulating layer as a gap material between two metal thin films to form a nanogap. For a nanogap array fabrication using atomic layer lithography, the ALD is the key process because an insulting layer is deposited along the surface of the first metal thin film patterned by photolithography [44]. This allows a formation of a metal-insulator-metal structure at the side walls of the pattern, as a nanogap with a vertical direction to the substrate. In addition, the nanogap size is directly defined by the thickness of the insulating layer determined by the number of cycles in the ALD process. Therefore, the atomic layer lithography can produce a nanogap array with various pattern structures, 1 nm-controllable gap size and large area pattern in wafer-scale by photolithography and ALD.

Figure 1 schematically represents the process of atomic layer lithography in a cross-sectional for a nanogap array fabrication. A gold (Au) thin film is firstly patterned on a substrate in large area by photolithography. ALD is then performed to deposit an alumina (Al_2O_3) layer as an insulator while controlling the number of cycles to set the thickness of the insulating layer. After that, a secondary Au layer is deposited and the excessive second Au layer on the first Au film is peeled off by an adhesive tape to completely form a nanogap array. A nanogap composed of a metal-insulator-metal structure is formed

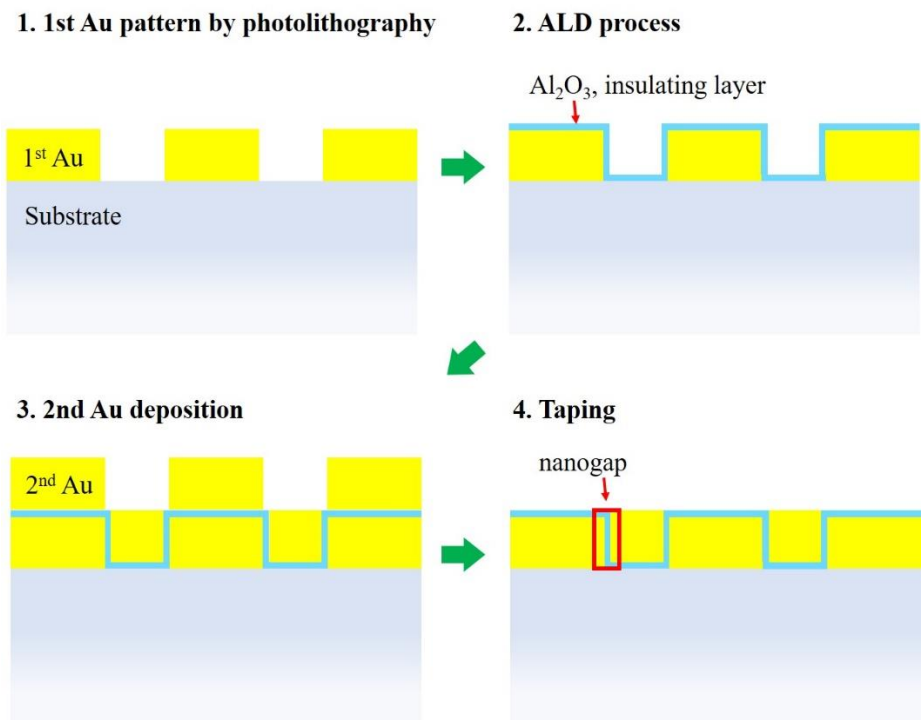

Figure 1. Atomic layer lithography for a nanogap array fabrication.

Schematic representation of atomic layer lithography for a nanogap array fabrication in cross-sectional. Au thin film on a substrate is patterned by photolithography. Subsequently, ALD is performed to deposit Al_2O_3 insulating layer with a desired thickness on the first Au pattern. a secondary Au layer is deposited on the patterned Al_2O_3/Au film. The nanogap array is finally completed by removing the excess Au layer on the first Au film using an adhesive tape. A nanogap composed of an Au- Al_2O_3-Au structure at a side wall is indicated in a red box. The gap size is determined by the thickness of Al_2O_3 layer in the ALD.

at the side walls of pattern, as indicated in a red box. Thus, the nanogaps are vertical to the substrate and the gap size is adjusted by the thickness of the Al_2O_3 insulating layer.

The advantages of atomic layer lithography for fabrication of a nanogap array can be a solution for the issues of a graphene gap prepared by the transfer method, as pointed out earlier. Based on atomic layer lithography, a graphene gap array can be prepared with vertical alignment and large area pattern.

2.2 Graphene synthesis by plasma enhanced CVD

Even though atomic layer lithography can adjust a gap size in 1 nm scale, it is hard to reduce the gap size to a sub-nanometer size due to the minimum thickness of an insulating film in ALD. In order to achieve a sub-nanometer gap, two-dimensional materials, such as graphene, hexagonal boron nitride (h-BN), molybdenum disulfide (MoS_2), and etc., can be suggested as a gap material since they are atomically thin. Among the two-dimensional materials, graphene is relatively useful because of its large area and single atomic composition.

As mentioned earlier, a graphene gap prepared by simple transfer method is inadequate for nanogap-based applications due to the limitations of horizontally formed gaps. Thus, a graphene gap array with a vertical orientation and large area pattern is required, similar to a nanogap array fabricated by atomic layer lithography. However, simply transferring graphene on a patterned metal thin film is hard to obtain a graphene gap with a vertical alignment, since the pattern is not conformally covered with graphene at all side walls. Therefore, a transfer-free route for a desired graphene gap array is a prerequisite.

According to the atomic layer lithography for fabrication of a nanogap array, an insulating layer is directly deposited along a

patterned metal thin film by ALD. Similar to this, graphene is typically synthesized on a whole area of copper (Cu) foil by chemical vapor deposition (CVD) [45]. The synthesis of graphene on a Cu foil by CVD is schematically illustrated in Figure 2. A methane (CH_4) gas, as a carbon feedstock, decomposes into carbon atoms by thermal and/or plasma energy in CVD. The carbon atoms are then adsorbed on the Cu surface due to the low carbon solubility of Cu. Subsequently, graphene is laterally grown on the Cu surface by bonding the carbon atoms each other [46]. It should be noted that the Cu acts as a metal catalyst to aid the decomposition of the CH_4 gas [47]. According to the mechanism of graphene synthesis in the CVD, a Cu thin film, instead of Cu foil, can be used as a metal catalyst for the decomposition of a CH_4 gas, as well as a patterned metal structure for a graphene gap array. Furthermore, graphene can be synthesized on the patterned Cu thin film by CVD. As a result, using CVD for graphene synthesis on a patterned Cu thin film can be sufficiently applied to atomic layer lithography by replacing ALD in which an insulating layer is deposited on a patterned metal film.

There are two types of CVD for graphene synthesis. The first is thermal CVD (TCVD), which uses only thermal energy to decompose reactants. The other is plasma enhanced CVD (PECVD),

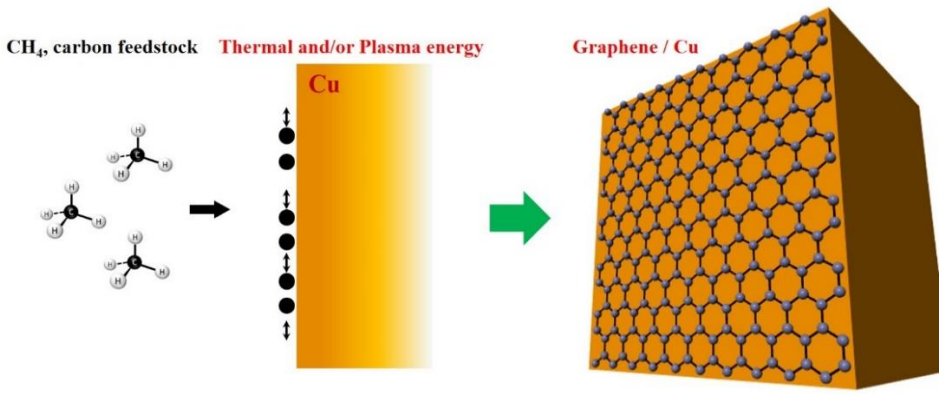

Figure 2. The synthesis of graphene on Cu surface by CVD.

Schematic illustration of graphene synthesis on a Cu surface. a CH_4 gas, as a carbon feedstock decomposes into carbon atoms by thermal and/or plasma energy in CVD. Carbon atoms are adsorbed on the Cu surface and freely move to laterally bond each other. Finally, graphene is grown on the whole of Cu surface.

which pyrolyzes reactants with a plasma assistant. Thus, the synthesis temperature of graphene varies depending on the CVD types. For TCVD, the typical synthesis temperature is 1000 – 1050 °C, near the melting point of bulk Cu. On the other hand, in the case of PECVD, graphene can be grown below 900 °C due to the help of hydrogen–methane plasma [48, 49]. To fabricate a graphene gap array using atomic layer lithography, a Cu thin film should be utilized for graphene synthesis. It is the fact that the melting temperature of Cu rapidly decreases, as the thickness of a Cu film decreases in nanometer scale [50]. Accordingly, PECVD is fairly appropriate rather than TCVD for synthesis of graphene on a Cu thin film.

In many cases, graphene is typically grown on Cu foils. However, in order to manufacture a graphene gap array, it is important to investigate synthesis mechanism of graphene according to the synthesis conditions in PECVD since a patterned Cu thin film should be in place of a Cu foil. As illustrated in Figure 3, the PECVD was implemented to demonstrate graphene synthesis with various synthesis conditions. The PECVD shown in Figure 3(a) mainly consists of a chamber for reaction, an inductively coupled plasma (ICP)–coil for generating plasma, and silicon carbide (SiC) rods for heating. Figure 3(b) describes the PECVD process and procedure graph for graphene synthesis. A Cu foil (25 ㎛ thick, 99.8 %, Alfa

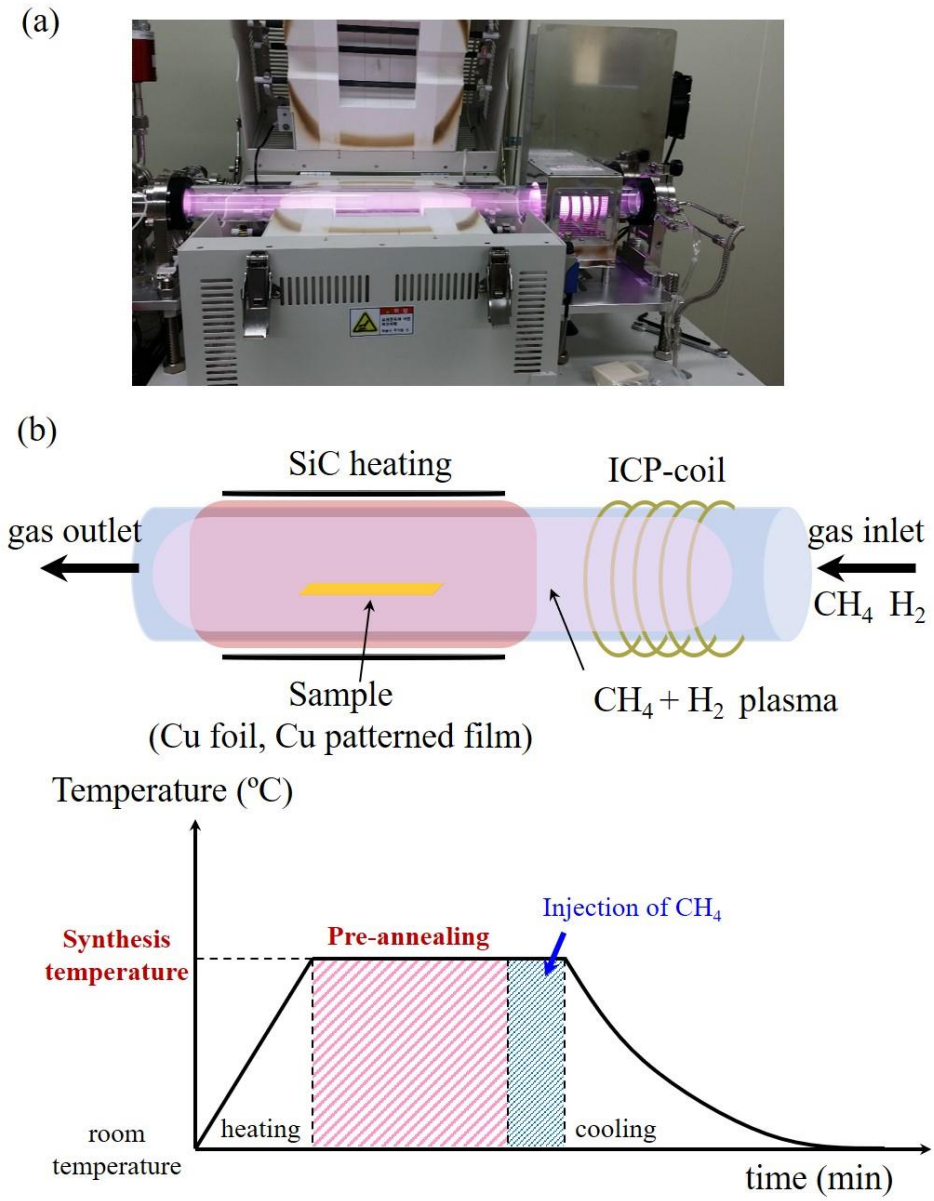

Figure 3. The PECVD process for graphene synthesis.

(a) A photograph of the PECVD used for graphene synthesis. (b) The schematic representation of the PECVD process (up) and procedure graph as a function of time (down).

Aesar) was firstly located at the center of the heating zone in the chamber. And the chamber was heated up by joule heating of SiC rods. At the same time, a hydrogen (H_2) gas with flow of 100 standard cubic centimeters per minute (sccm) was injected into the chamber. During the heating-up, the Cu foil was pre-cleaned with H_2 plasma generated by applying a radio frequency (RF) of 13.56 MHz to the ICP-coil. When the chamber reached the target temperature, the Cu foil was pre-annealed while introducing H_2 without generating plasma. In the pre-annealing process, the surface of the Cu foil is smoothened, which results in graphene with a high quality [51, 52]. After the pre-annealing process, CH_4 with a flow rate of 1 sccm was additionally supplied into the chamber for 30 sec to synthesize graphene on the Cu surface with generating the H_2-CH_4 plasma. The working pressure of the chamber was 1.4 torr. After the synthesis of graphene, the chamber was then cooled down to room temperature while introducing the H_2 only. The synthesis temperature and pre-annealing time were adjusted to 700 – 900 °C and 0 – 90 min, respectively. The plasma power was fixed at 300 W. In order to evaluate the graphene synthesized at each condition in the PECVD, the graphene on the Cu foil was transferred onto a 300 nm thick SiO_2/Si substrate using a wet-transfer method [30]. To transfer the graphene synthesized on the Cu foil, poly(methyl-methacrylate)

(PMMA) was spin-coated on the graphene/Cu foil at 3000 rpm for 30 s. The Cu foil was then etched out by Cu etchant ($FeCl_3$ solution) diluted in deionized-water (DI-water). The PMMA/graphene was rinsed with the DI-water and placed on the SiO_2/Si substrate. The graphene on the SiO_2/Si was finally obtained by removing the PMMA with acetone.

In Figure 4, graphene synthesized at various temperatures with pre-annealing time of 60 min is observed in naked eye by optical contrast due to a multiple reflection [53]. It is found that the graphene is uniformly synthesized on the whole Cu area. In addition, the optical contrast increases as a decrease in the synthesis temperature, which implies increasing the number of graphene layers. These results provide that the graphene synthesis conditions in the PECVD can be sufficiently adopted to a patterned Cu thin film for fabrication of a graphene gap array. The structural features of graphene synthesized at each condition will be discussed in detail in chapter 3.

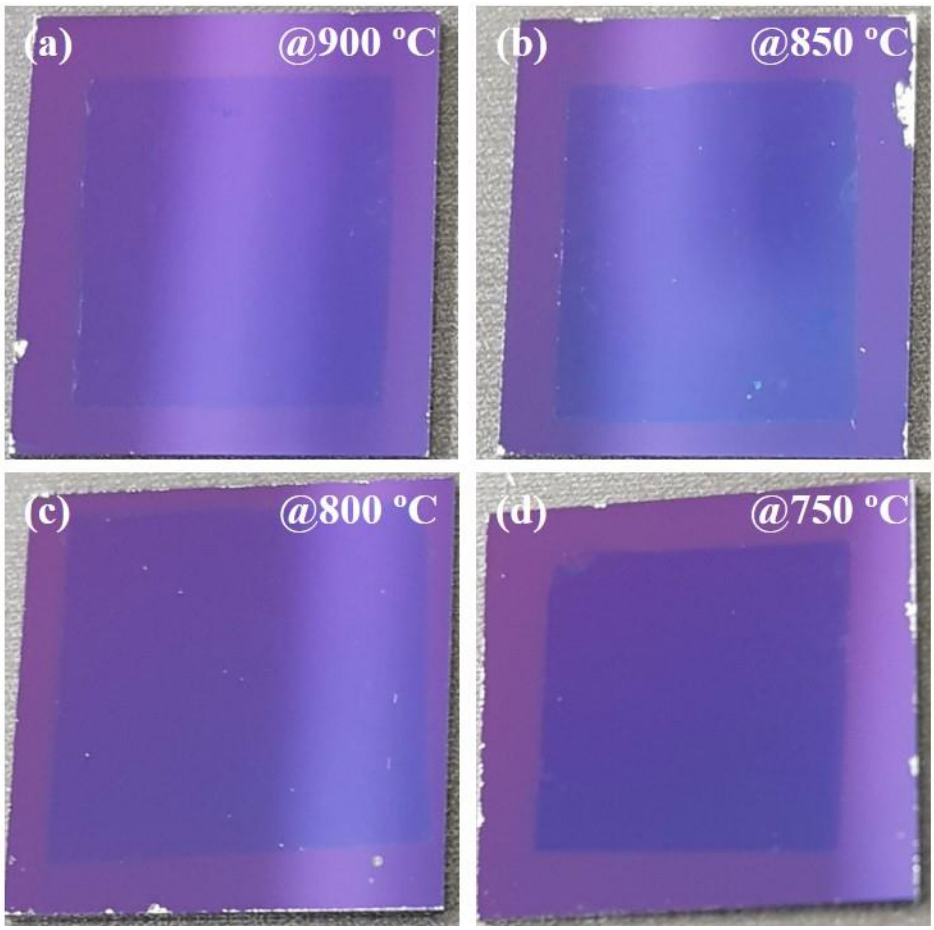

Figure 4. The graphene on the SiO_2/Si substrate.

Photograph images for graphene transferred on a SiO_2/Si substrate. The graphene synthesized at (a) 900 °C, (b) 850 °C, (c) 800 °C, and (d) 750 °C with pre-annealing time of 60 min in the PECVD was transferred on a SiO_2/Si substrate by wet transfer method.

2.3 Fabrication of a graphene gap array

For fabrication of a graphene gap array by using atomic layer lithography, graphene synthesis should be implemented on a patterned Cu thin film. As mentioned earlier, a melting point of Cu thin film with a nanometer scale thickness is much lower than that of bulk Cu. Thus, it is necessary to investigate that a patterned Cu thin film can withstand high temperature in the PECVD before graphene synthesis. It is well known that a metal thin film is melted from its surface and toward the inside sequentially as temperature rises up. It means that the next inside layer will be melted after the outer layer melted [50]. Therefore, it is expected that the surface of a patterned Cu thin film would be damaged during graphene synthesis due to the high synthesis temperature in the PECVD.

In order to demonstrate the deformation of a patterned Cu thin film, the annealing process was performed for 30 min at various temperatures of 750 °C to 900 °C, as the same temperature in graphene synthesis on a Cu foil by the PECVD. A patterned Cu thin film with 400 nm thickness was prepared by photolithography. The pattern is stripes with a period of 100 ㎛ and a linewidth of 50 ㎛. Figure 5 shows the optical microscope images for the patterned Cu thin film annealed at various temperatures. It is found that the pattern was well maintained at all temperatures but the surface of Cu was

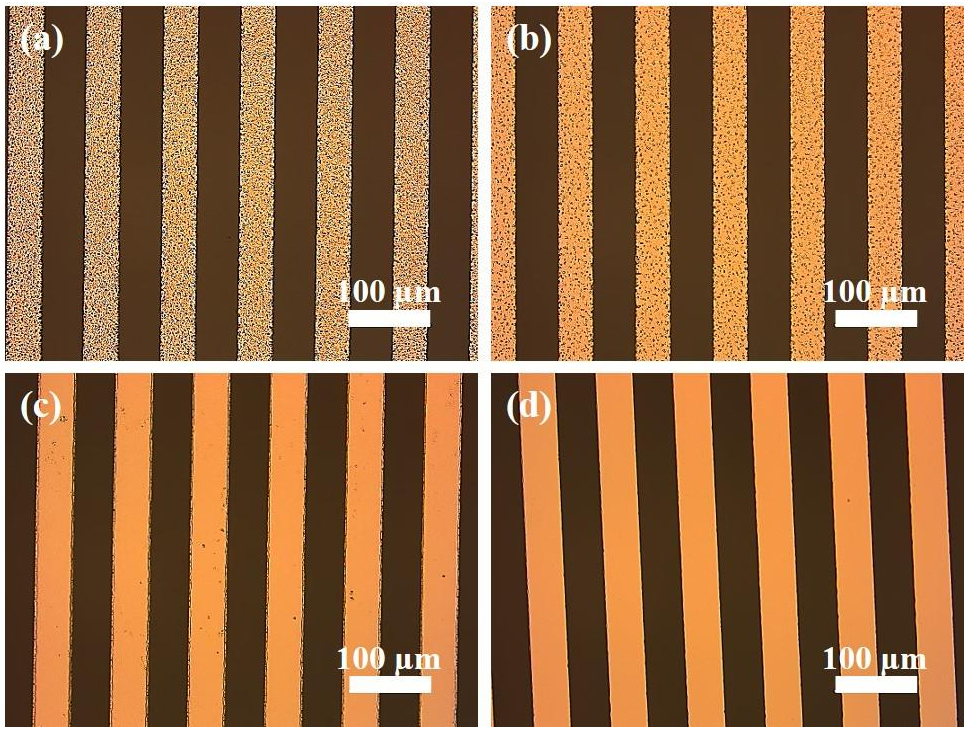

Figure 5. The patterned Cu thin film annealed at various temperatures.

Optical microscope images of the patterned Cu thin film annealed at (a) 900 °C, (b) 850 °C, (c) 800 °C, and (d) 750 °C for 30 min.

varied with respect to the temperatures. Below 800 ℃, the smooth Cu surface is observed, while the Cu pattern becomes rough above 850 ℃ due to the surface melting. Also, the roughness of the Cu surface further increases as the temperature increases.

In order to precisely measure the surface roughness of the annealed Cu thin film, atomic force microscope (AFM) with non-contact mode was carried out. Figure 6 exhibits the AFM images and line profiles collected from the edge of a Cu pattern. Below 800 ℃, the smooth surface morphology of Cu thin film is observed, indicating that the patterned Cu thin film is barely affected by the annealing, as shown in Figure 6(c) and 6(d). However, the surface morphology of the Cu thin film annealed above 850 ℃ becomes very rough by melting and agglomeration in some parts of the surface of the pattern, which is consistent with the results of the optical microscope measurements. The line profile indicated by the red line in the AFM image shows the surface roughness of the annealed Cu film. For the line profiles in Figure 6(a) and 6(b), the surface roughness of the Cu film annealed at 850 ℃ and 900 ℃ is measured to be tens of nm and around 100 nm, respectively. Meanwhile, below 800 ℃, the surface roughness of the Cu is nearly smooth, which implies that the Cu surface is barely affected at these temperatures.

It is noted that the side walls of the pattern are employed for

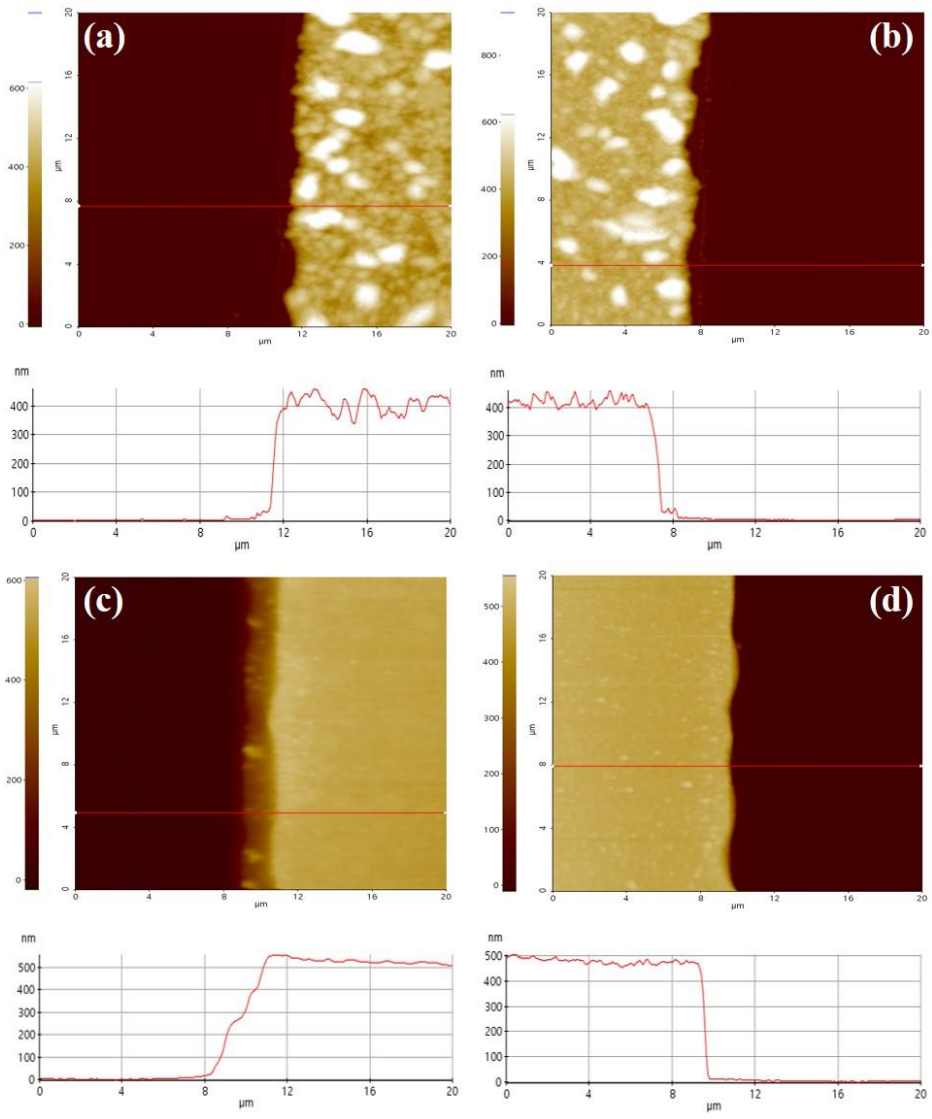

Figure 6. The AFM measurement for the annealed Cu thin film.

Surface morphology and roughness by the AFM measurement for the patterned Cu thin films annealed at (a) 900 °C, (b) 850 °C, (c) 800 °C, and (d) 700 °C.

a graphene gap array with the vertical direction to a substrate, composed of Cu−graphene−Cu structure. Regarding the AFM results, graphene synthesis in the PECVD can be implemented at the temperatures up to 850 °C for a patterned Cu film with 400 nm thickness since the roughness of Cu surface annealed at 900 °C is insufficient.

Based on the demonstrations of the graphene synthesis and annealing a Cu thin film in the PECVD, atomic layer lithography was finally performed to fabricate a graphene gap array, as described in Figure 7(a). First of all, standard photolithography is conducted to pattern a Cu thin film on a quartz substrate using the image reversal method. The image reversal method in photolithography is mostly used for patterning a metal thin film because a photoresist (PR) is remained with an undercut on a substrate after development for effective lift−off of the metal thin film. The following is a brief description of the photolithography for patterning a Cu thin film. the PR, AZ5214E, was spin coated on a quartz substrate at 4000 rpm for 60 sec. The PR/quartz substrate was then baked at 90 °C for 60 sec to remove the solvent in the PR. UV light (λ = 365 nm) with a dose of 150 $mJ \cdot cm^{-2}$ was subsequently illuminated to the PR/quartz substrate below a photomask to form a pattern on the PR. In the case of image reversal, the first exposed area of PR is remained after

development so that metal thin film has the same pattern as the photomask. For a graphene gap array, two photomasks were used. One is a stripe pattern with 100 ㎛ pitch and 50 ㎛ linewidth. And the other pattern is a square array with 50 x 50 $㎛^2$. After the first UV exposure, the sample was baked again at 120 ℃ for 120 sec. At this time, by the reversal bake, the first exposed PR area was cross-linked while the unexposed area remains photoactive. Then, flood exposure with a dose of 1500 mJ · cm^{-2} was conducted without the photomask to make the unexposed PR soluble in developer. Afterwards, the sample was immersed in MIF 500 developer for 60 sec and rinsed with DI-water so that the PR area exposed to the first UV light was remained. A 400 nm thick Cu thin film was deposited on the patterned PR/quartz substrate using a thermal evaporator. The patterned Cu thin film was finally obtained by lift-off with acetone. For the next step, it was placed at the center of the heating zone in the chamber in the PECVD. In order to synthesize graphene on the patterned Cu thin film, the PECVD process was carried out with the same conditions as graphene synthesis on the Cu foil. Firstly, the chamber was heated up to the synthesis temperature with 100 sccm H_2 flow. During the heating-up, the H_2 plasma was generated to clean the patterned Cu thin film. When temperature reached, the pre-annealing was performed for 30 min without H_2 plasma. Then, CH_4

with 1 sccm flow was injected into the chamber for 30 sec to grow graphene on the Cu surface. At that time, H_2–CH_4 plasma was generated to help the decomposition of the CH_4 gas into carbon atoms and hydrocarbon radicals. After synthesis, the plasma generation and the injection of CH_4 gas were tuned off and the chamber was naturally cooled down to room temperature while introducing the H_2 gas.

After graphene synthesis on the first patterned Cu thin film, a secondary Cu layer was deposited on the patterned graphene/Cu film by the thermal evaporator to form a graphene gap array with a vertical alignment at the side walls of the pattern. It should be noted that if the thickness of the second Cu layer is the same as the first layer, it is hard to measure the THz transmission due to the optically thick Cu layer and the very small gap size. Therefore, the second Cu layer should have much smaller thickness rather than the first Cu thin film. By this reason, the thickness of the second Cu layer deposited was set to be 50 nm for the measurement of optical properties of the graphene gap array at THz regime.

The final step in atomic layer lithography for a nanogap array fabrication is typically the removal of the excessive second layer on the first metal thin film by using an adhesive tape. In most cases, since the second metal layer has the same thickness as the first metal layer, a flat nanogap array is finally obtained as shown in Figure 1.

However, for the manufactured graphene gap array, difference in thickness between the first Cu layer and the second Cu layer is quite large. Furthermore, the side walls of the pattern are imperfectly vertical to the quartz substrate, causing the gap regions are closed by covering with the second Cu layer during the deposition. In this situation, taping process cannot be appropriate for completing the fabrication of the graphene gap array since peeling off the whole second Cu layer. This is why another step, instead of taping is required to open the gap regions while maintaining the Cu–graphene–Cu structure at the side walls. For this, Ion milling system was employed to remove only the Cu layer covering the gap regions. Argon (Ar) ions accelerated with a voltage of 400 V were incident to the sample rotating with 9 rpm at slanted angle of 85° for 10 min. Finally, in Figure 7(b) and 7(c), the graphene gap slit and square slot array were completely obtained. It is hard to directly observe the graphene gap in an optical microscope, but the interfaces, which are considered as the gap regions between the first and second Cu layers, are readily distinguishable due to the difference in the surface morphology. Demonstrations of the structures and the optical properties for the graphene gap array prepared by atomic layer lithography will be discussed in the chapter 3 and 4.

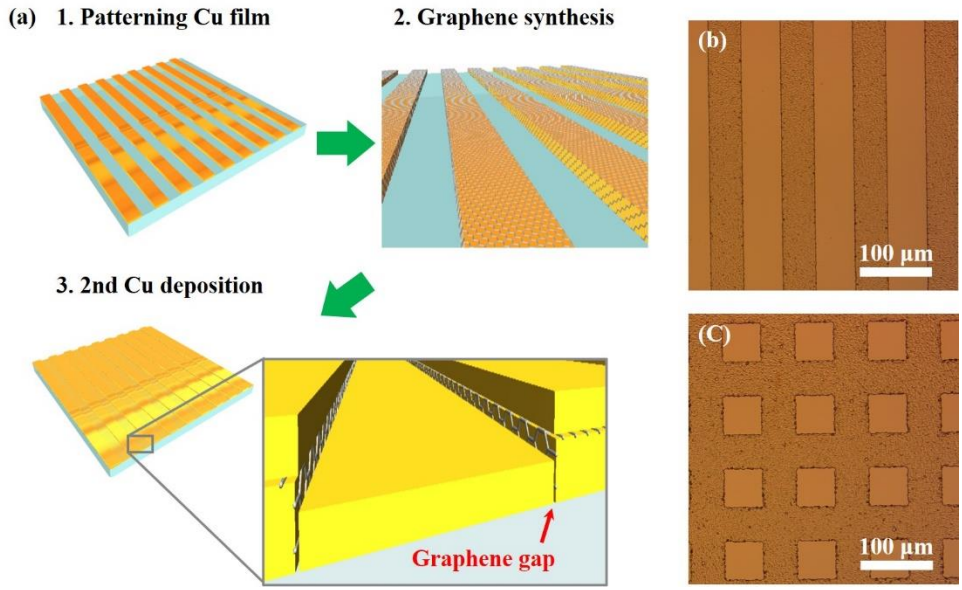

Figure 7. The fabrication of a graphene gap array.

(a) The schematic representation of the fabrication of a graphene gap array using atomic layer lithography. The patterned Cu thin film was prepared by photolithography. graphene was then synthesized on the patterned Cu film by the PECVD. The graphene gaps at the side walls of the pattern were formed after the secondary Cu layer deposition. Additional milling process was conducted to open the graphene gap regions covered with the second Cu layers. (b-c) The optical microscope images of the completely fabricated graphene gap (b) slit and (c) square slot array.

Chapter 3. Structural characterization of graphene gap

Field enhancement which is one of the significant characteristics for a nanogap is strongly dependent on the gap size. It is the fact that the size of a nanogap fabricated by atomic layer lithography is directly determined by the thickness of an insulating layer deposited by ALD. For a graphene gap array, graphene can be either a single-layer or a multi-layer graphene depending on the synthesis conditions in the PECVD. It means that a gap size is defined by a multiple of van der Waals distance according to the number of graphene layers. In this chapter, the structural features of the graphene gap array will be discussed in detailed.

3.1 Raman measurement of the graphene

Raman spectroscopy is a power tool to investigate graphene-related materials [54, 55]. Figure 8 shows a typical Raman spectrum for single-layer graphene as an example. Typically, there are three prominent peaks observed at ~1350 cm^{-1}, ~1590 cm^{-1}, and ~2684 cm^{-1} corresponding to the D-band, G-band, and 2D-band, respectively. The D-band is related to the disorder of graphene. The G-band associated with a first order Raman scattering involves an

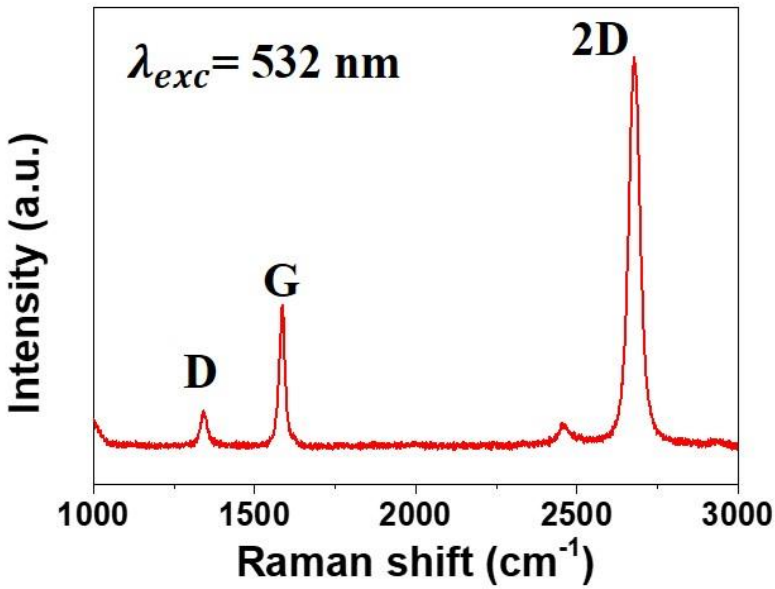

Figure 8. A Raman spectrum for single-layer graphene.

A Raman spectrum for single-layer graphene measured by an excitation laser of 532 nm wavelength. Three peaks are mainly observed at 1347 cm^{-1} (D-band), 1588 cm^{-1} (G-band), and 2687 cm^{-1} (2D-band). Compared to the G-band intensity, the D-band has low intensity and the 2D-band is a high and sharp peak.

electron and the doubly degenerated phonons (iTO and iLO) at the center of the Brillouin zone which is typically observed for graphene-related materials. The 2D-band from an intervalley double resonance Raman scattering involves an electron and two iTO phonons at the K point. For single-layer graphene, low intensity of D-band and high intensity of 2D-band are typically observed compared to the intensity of G-band. In the case of multi-layer graphene, a 2D-band peak becomes lower and broader, as the number of graphene layer increases [56]. Thus, the number of layers and quality for graphene can be estimated using the 2D-band full width at half maximum (FWHM), the intensity ratios of 2D-band to G-band (I_{2D}/I_G), and D-band to G-band (I_D/I_G). It is noted that the I_{2D}/I_G and I_D/I_G are calculated using the peak area. The I_D/I_G provides a grain size of graphene according to the following equation [57]

$$L_a = C(\lambda)/(I_D/I_G)$$

where L_a (nm) is the grain size, λ (nm) is the wavelength of incident light, and $C(\lambda) = 2.4 \times 10^{-10}\lambda^4$ is the calculated value.

Firstly, in order to evaluate the graphene synthesized on the Cu foil using the PECVD, a Raman spectrum was collected from the graphene transferred on SiO_2/Si substrate shown in Figure 4 using a Renishaw inVia Raman microscope equipped with an excitation laser

of 514 nm wavelength. The incident laser power irradiated on the samples was adjusted to 30 mW · cm^{-2}. In Figure 9(a), Raman spectra was measured from the graphene synthesized at various temperature with pre-annealing time of 90 min as described in the section 2.2. The D-band, G-band, and 2D-band are located at 1347 cm^{-1}, 1588 cm^{-1}, 2687 cm^{-1}, respectively. The Raman spectrum for the graphene synthesized at 900 °C reflects typical single-layer graphene features involving a negligible intensity of the D-band and high intensity of the 2D-band. For the graphene synthesized at 850 °C, the Raman spectrum indicates single-layer graphene with a little high intensity of D-band. Below the synthesis temperature of 850 °C, D'-band caused by a weak disorder of graphene appears at ~1625 cm^{-1}. When decreasing the synthesis temperature, the intensities of the D- and D'-bands increase simultaneously while that of the 2D-band decreases. It means that multi-layer graphene is synthesized below 800 °C. However, at 700 °C, the 2D-band eventually disappears, implying amorphous carbon formation on the Cu surface [55]. Figure 9(b) indicates Raman spectra measured from graphene synthesized at 900 °C with various pre-annealing times. Without the pre-annealing procedure, the Raman spectrum of synthesized graphene reveals high intensity of the D-band and small intensity of the 2D-band, which is similar to that of multi-layer

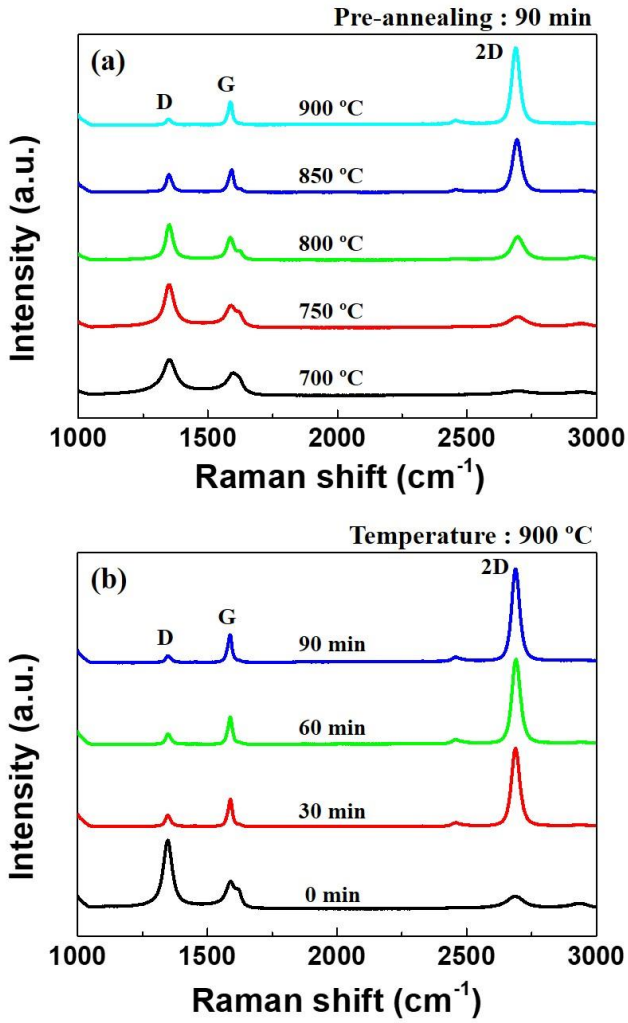

Figure 9. The Raman spectra for the graphene synthesized on the Cu foil by the PECVD.

(a) Raman spectra obtained from graphene synthesized at various synthesis temperatures. The pre-annealing was fixed for 90 min. (b) Raman spectra measured from graphene synthesized with various pre-annealing time. The synthesis temperature was fixed at 900 °C.

graphene. However, when the pre-annealing time is prolonged above 30 min, typical Raman features for single-layer graphene are clearly observed. Therefore, it is found that the synthesizing graphene on the Cu surface is highly affected by the pre-annealing process.

The intensity ratios (I_D/I_G, I_{2D}/I_G), grain size, and 2D-band FWHM are presented in terms of synthesis temperature in Figure 10. In order to obtain the average values, Raman spectra was collected from five different locations for each sample. It is well known that the simultaneous modulation of decrease in the I_{2D}/I_G and increase in the 2D-band FWHM, which implies an increase in the number of graphene layers [54, 56]. By increasing the synthesis temperature from 750 ℃ to 900 ℃, the I_D/I_G and 2D-band FWHM both decreases, whereas the I_{2D}/I_G and grain size both increases. These results suggest that the temperature manipulation enables control of graphene layer number. The grain sizes for single-layer graphene synthesized at 900 ℃ and multi-layer graphene synthesized at 800 ℃ are estimated to be ~48 nm and ~12 nm, respectively. Along with the synthesis temperature of graphene, the pre-annealing process is a crucial factor for optimizing graphene synthesis [52, 58]. Figure 11 show I_D/I_G and I_{2D}/I_G statistically obtained from Raman spectra collected for five points of each graphene synthesized with various pre-annealing times. Above 30 min, the intensity ratios

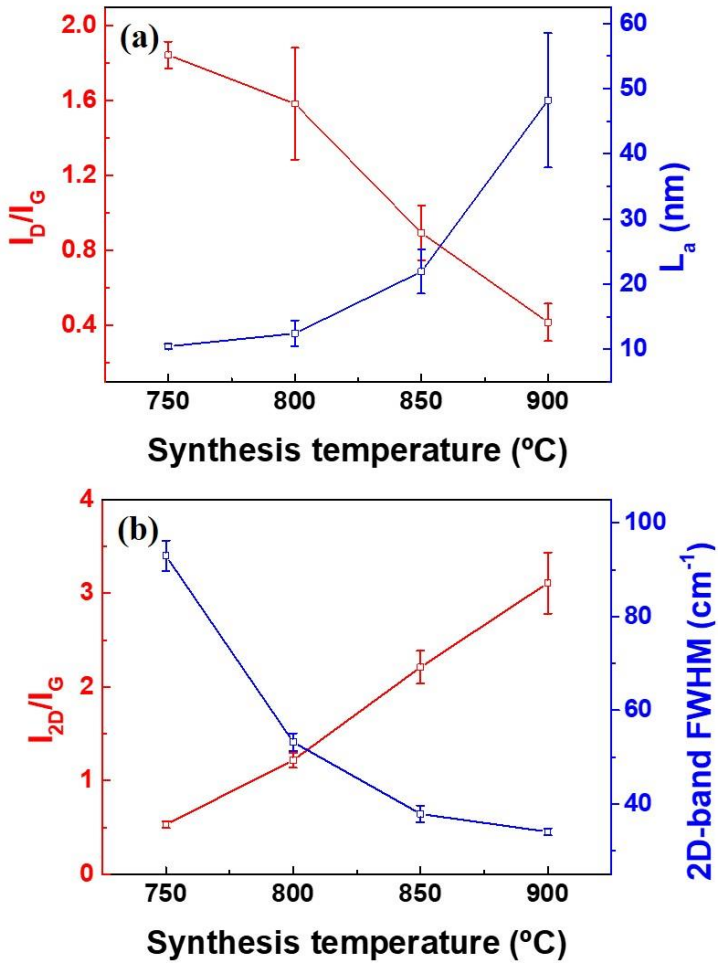

Figure 10. Intensity ratios, grain size, and 2D-band FWHM for the graphene synthesized at various temperatures.

The statistically obtained (a) I_D/I_G and grain size, (b) I_{2D}/I_G and 2D-band FWHM as a function of synthesis temperature.

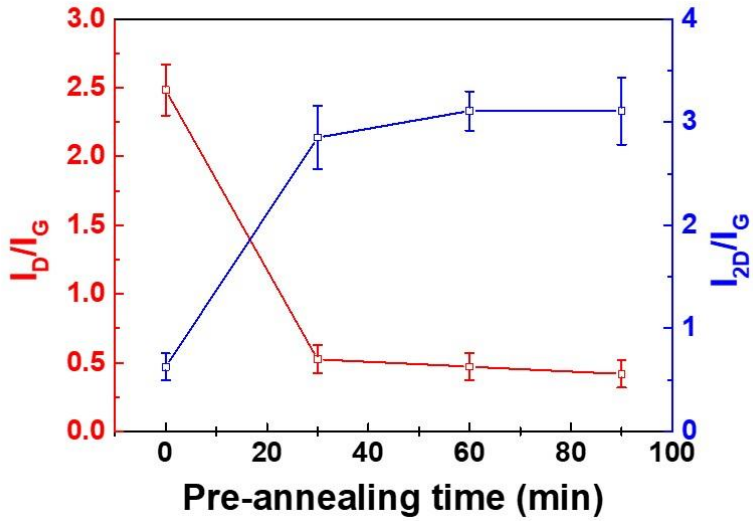

Figure 11. Intensity ratios for the graphene synthesized with various pre-annealing times.

The intensity ratios (I_D/I_G and I_{2D}/I_G) for the graphene synthesized with various pre-annealing times. Above 30 min, the both I_D/I_G and I_{2D}/I_G are saturated.

(I_D/I_G, I_{2D}/I_G) are saturated, which is in consistent with the Raman measurement in Figure 9(b). The Cu surface is initially very rough and partially oxidized, which results in environments for synthesizing multi-layer graphene rather than single-layer graphene. By performing the pre-annealing process, the Cu surface is gradually smoothened and a reduction of the Cu surface occurs. This leads to the synthesis of single-layer graphene with a relative high quality on the Cu surface [59].

Based on the Raman results, the graphene synthesis on the Cu surface will be discussed by comparing the synthesis conditions. Figure 12 schematically illustrates the graphene synthesis on Cu surface by carbon atoms and Hydrocarbon (CH_x) radicals in the PECVD. The CH_x radicals and carbon atoms are initially generated by the H_2-CH_4 plasma and migrate along the Cu surface to form the graphene layer. Generally, the CH_x radicals prevent carbon atoms attachment at graphene edges while the carbon atoms contribute to graphene growth [46, 47]. Furthermore, the catalytic activity of Cu to dissociate CH_x radicals is strongly dependent on the synthesis temperature [49]. Adequate synthesis temperatures and pre-annealing time of the Cu surface eliminate the negative effects of CH_x radicals by dissociating C–H bond on the Cu surface so that the carbon atoms increase significantly and preferably move on the Cu

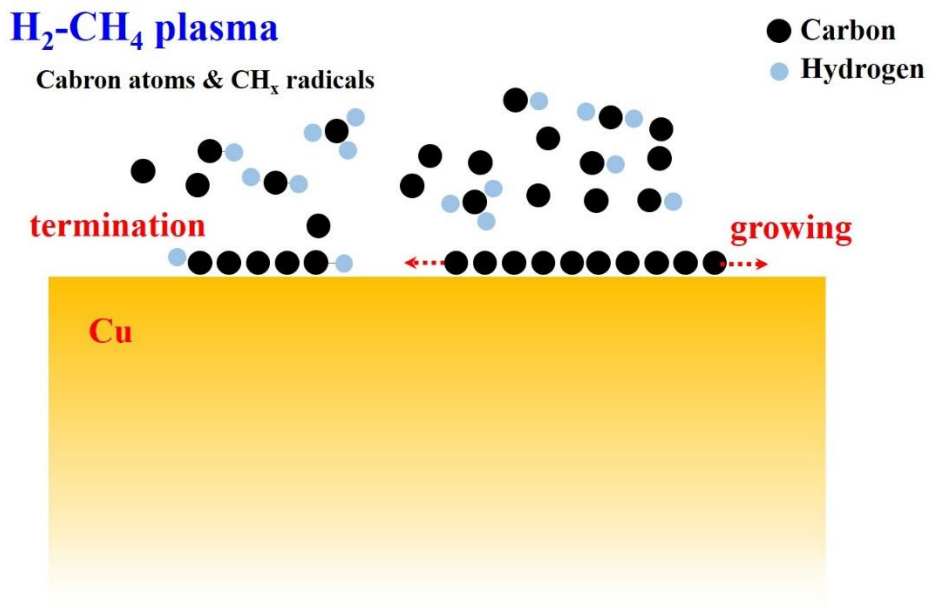

Figure 12. The synthesis mechanism of graphene on Cu surface in PECVD.

Schematic illustration for graphene synthesis in the PECVD. Graphene is laterally grown by attaching carbon atoms at edges, continuously. However, CH_x radicals attached at the edge prevents the growth.

surface in relatively high temperature to grow single-layer graphene with large area. However, the catalytic capability of Cu for dissociating the C–H bond declines gradually at lower temperature, which results in an increase of the CH_x radicals prohibiting the graphene layer growth laterally. In addition, the carbon atoms are unable to bind to the edges of graphene layer terminated by the CH_x radicals, thereby synthesizing another graphene layer on the previously grown graphene layer. As a result, the multi-layer graphene with a small grain size is preferably synthesized on the Cu surface at relatively low temperature.

By the analysis for graphene synthesis on the Cu surface, the graphene synthesized on the patterned Cu thin film can be also characterized with the same structural features since the same conditions in the PECVD was universally adopted. However, the surface roughness of a patterned Cu thin film significantly increases during the graphene synthesis using the PECVD due to the annealing process. The increase in the surface roughness of Cu may affect the graphene synthesis. In order to evaluate the graphene synthesized on the patterned Cu thin film before the secondary Cu deposition, Raman spectroscopy measurement was implemented with 532 nm excitation wavelength. The incident laser with a power of 10 mW and 1 μm spot size was focused on the sample through a handmade Raman

spectroscope which consists of a modified microscope, high-pass filter, lenses, and a spectrometer on an optical table. The Raman signals scattered from the sample in a backscattering geometry was collected by the objective lens and sent to the spectrometer with integration time for 60 sec.

In Figure 13, the red and blue curves correspond to representative Raman spectra for the graphene synthesized on the patterned Cu thin film at 850 ℃ and 750 ℃, respectively. Since discernible baselines are due to the Cu fluorescence, the relatively small Raman signals from the samples are observed. It is the fact that Raman measurement for graphene is considerably affected by a substrate [60, 61]. Compared to the graphene fingerprints indicated by guide lines, the red curve implies single-layer graphene features and the blue curve with relatively high D-band indicates multi-layer graphene. The black curve is a Raman spectrum measured from the quartz substrate exposed between the Cu patterns. No meaningful graphene features in the Raman spectrum are observed, indicating that graphene is solely synthesized on the Cu pattern.

According to the Raman results, the graphene is conformally on the patterned Cu thin film by the PECVD. Also, the number of graphene layers can be adjusted by the synthesis conditions which can be commonly adopted to the PECVD for both Cu foil and Cu thin

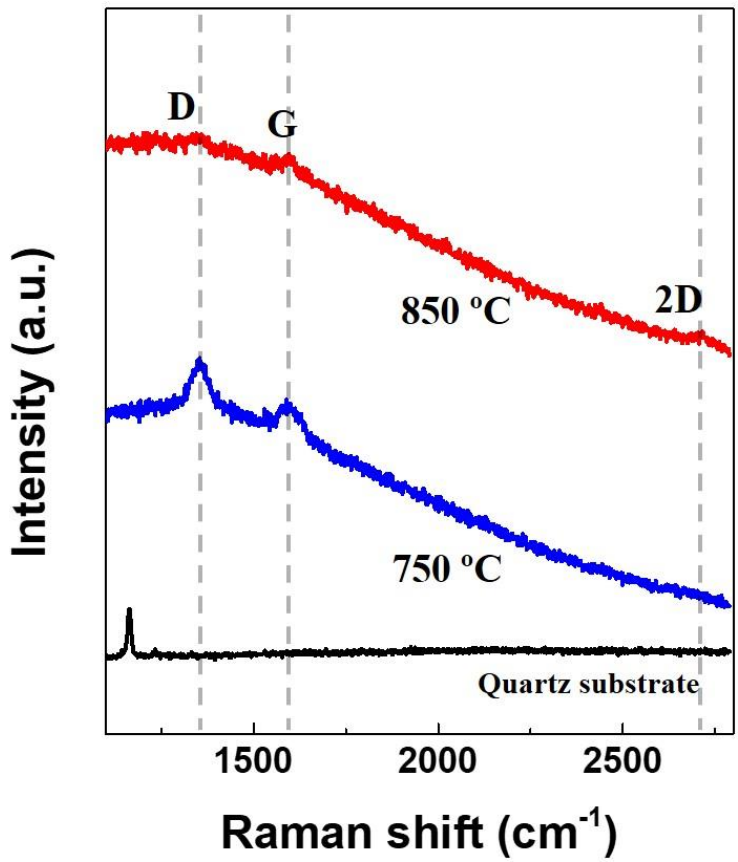

Figure 13. The Raman spectra for the graphene on the patterned Cu film.

Raman spectra collected from the graphene synthesized at 850 °C (red) and 750 °C (blue) on a patterned Cu film. The black curve is measured from the exposed quartz region between the Cu patterns, indicating that graphene is only synthesized on the Cu surface.

film. Therefore, the fabricated graphene gap array is composed of single-layer or multi-layer graphene, associated with the synthesis conditions in the PECVD. Furthermore, it is expected that the gap size is decided by a multiple of van der Waals distance according to the number of graphene layers.

3.2 Defining the size of the graphene gap

In the case of nanogap by atomic layer lithography, the typical gap size is defined by the thickness of the insulating layer associated with the number of cycles in the ALD process. It is unnecessary to directly observe a gap region to estimate the gap size. However, the results of the Raman spectroscopy for the graphene on the patterned Cu film only indicate that the graphene gap array consists of single-layer or multi-layer graphene depending on the synthesis conditions in the PECVD. Therefore, in order to accurately define the size of the graphene gap, it is important to figure out the number of graphene layers. Field emission-scanning electron microscope (FE-SEM) and Cs-corrected transmission electron microscope (Cs-TEM) was carried out to directly observe graphene layers in a gap region. For obtaining a graphene gap region sample, FIB was utilized to cut the graphene gap array into cross-section. The SEM images in Figure 14(a) and 14(c) display the cross-sectional view of the graphene gap synthesized at 850 °C and 750 °C. It is found that the graphene gap is completely fabricated with a vertical direction to the quartz substrate by atomic layer lithography including the ion milling process, as expected. The interface between the first and second Cu thin film is distinguished by the difference in the thickness of the Cu layer, which indicates the gap region blurry captured as a line in a

red box in the SEM image due to the very small gap size. In Figure 14(b) and 14(d), the TEM images show the graphene gap corresponding the SEM images, precisely. It is clearly observed that the graphene gap uniformly formed along the Cu surface. Furthermore, the black lines indicating the graphene layers at the gap can provide the information of the number of graphene layers for the single-layer and multi-layer graphene, depending on the synthesis conditions in the PECVD. This indicates that TEM results in terms of their number of layers coincide with the Raman results. As a result, the gap size can be directly measured by the TEM observation.

In contrast to a nanogap size determined by the thickness of an insulating layer, the gap size for the graphene gap is defined as the distance between the Cu layers since the distance of Cu-graphene is also the van der Waals distance. Therefore, the size of graphene gap is defined by a multiple of van der Waals distance associated with the number of graphene layer. In the case of the single-layer graphene gap, the gap size was measured to be approximately 0.67 nm in the TEM. In fact, the single-layer graphene gap consists of a double van der Waals distance, which seems to be reasonable compared to previously reported graphene gap size [62]. For the multi-layer graphene gap which consists of six graphene layers in Figure 14(d), the gap size is approximately

2.38 nm, which indicates seven times larger than the van der Waals distance. Consequently, the gap size for a graphene gap array can be adjusted from the minimum size of 0.67 nm, according to the number of graphene layers. This means that the graphene gap array has a perfect a sub-nanometer gap with a vertical alignment for single-layer graphene gap and the gap size can be controlled by the van der Waals distance with adjusting the number of graphene layers.

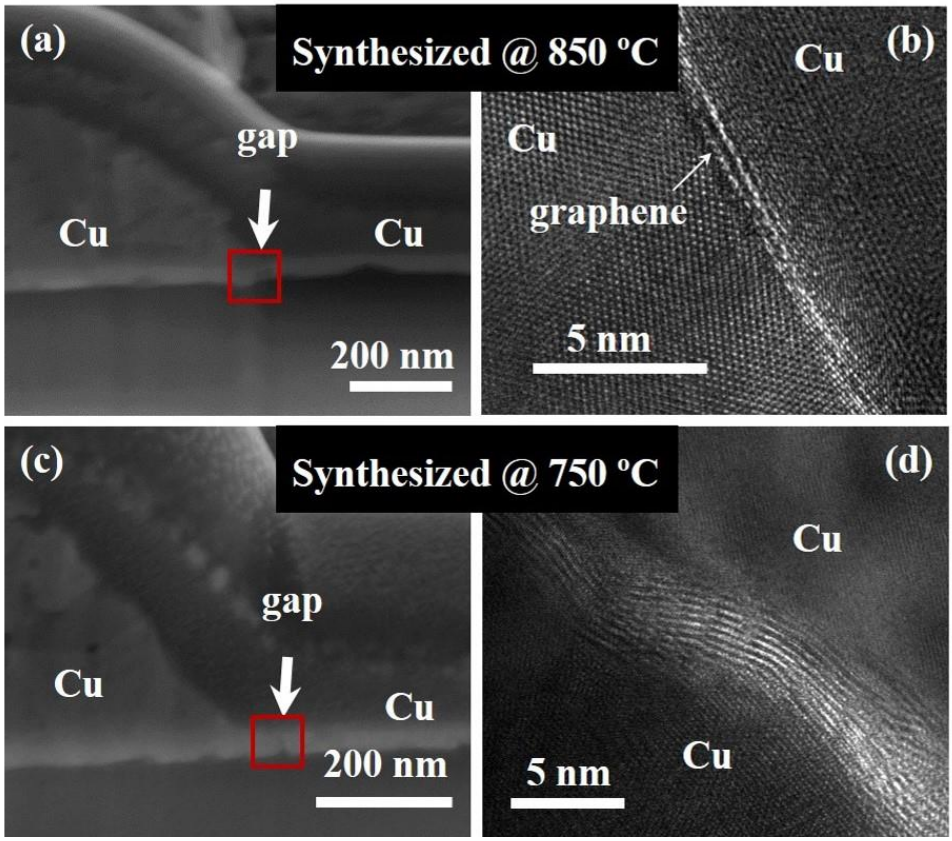

Figure 14. The SEM and TEM measurements for the graphene gap.

(a-b) For the single-layer graphene gap, the (a) SEM and (b) TEM images. (c-d) (c) SEM and (d) TEM images of the multi-layer graphene gap, which is composed of six graphene layers.

Chapter 4. Optical properties of graphene gap array at THz regime

For the graphene gap array prepared with a vertical orientation to the substrate, it is possible to quantify field enhancement and electric fields formed inside the gap at THz waves. In addition, the electric fields formed inside the gap can interact with the graphene layer. In this chapter, Optical properties of the graphene gap slit array at THz regime will be discussed using THz-time domain spectroscopy.

4.1 THz-time domain spectroscopy

In order to explore the optical properties of the graphene gap array at THz regime, the THz-time domain spectroscopy was performed, as described in Figure 15. In the THz-time domain spectroscopy, a mode-locked femtosecond Ti:sapphire laser operating at a 80 MHz repetition rate and a pulse duration of 130 fs at 800 nm is split into two beams for THz generation and detection. One beam is illuminated on a biased gallium arsenide (GaAs) emitter to generate a THz pulse with a maximum field of ~10 V cm^{-1} at the focus. The THz pulse are collected by parabolic mirrors before it is focused on a sample. Then, the THz pulse is normally transmitted

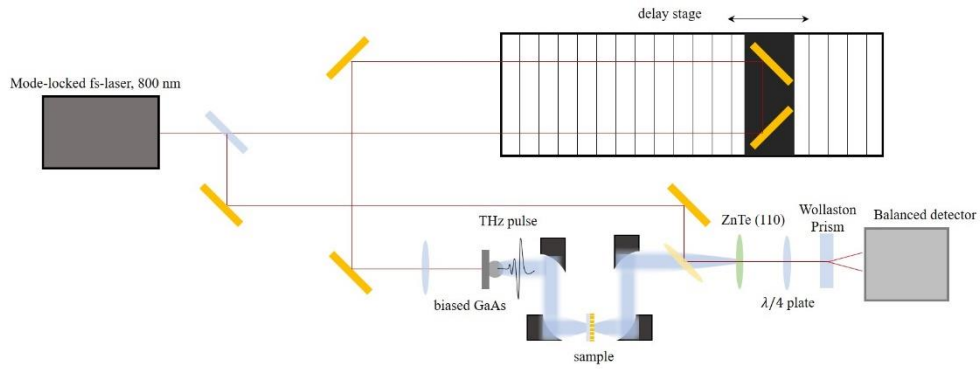

Figure 15. The THz-time domain spectroscopy.

Schematic setup image for THz-time domain spectroscopy used to measure the THz transmission of a graphene gap slit array. THz waves are generated using biased-GaAs irradiated by mode-locked femtosecond Ti:sapphire laser. And the THz waves are focused on a sample by parabolic mirrors. The transmitted THz waves are focused at ZnTe crystal for electro-optic sampling.

through a sample. The transmitted THz waves are collected using parabolic mirrors and detected via electro-optic sampling using a zinc telluride (ZnTe) crystal with (110) orientation.

In the electro-optic sampling, when the THz wave is focused on the ZnTe crystal, the index of refraction of the ZnTe crystal is varied depending on the electric field intensity of the THz wave. At this time, the other split femtosecond laser is illuminated on the ZnTe crystal and its polarization is changed according to the index of refraction of the ZnTe crystal. Subsequently, the beam is passed through a quarter wave plate and a Wollaston prism, which leads to separate into parallel and perpendicular polarized beams. The electric field intensity of THz wave is then measured by the difference in intensity of the two polarized beams at a balanced detector. The THz wave in time domain is measured by moving the delay stage. Furthermore, the amplitude and phase in frequency domain for the THz waves are obtained by Fourier transformation of the THz waves in the time domain.

4.2 Kirchhoff integral and field enhancement

The Kirchhoff integral formalism is useful to demonstrate near field enhancement of subwavelength structures measured in a far field by using a reference aperture [63]. The relationship between near field and far field is derived from the Kirchhoff integral formalism. Figure 16 illustrates a geometry of experiment with a reference aperture illuminated by an incident electric field. When an electric field with the horizontal polarization is incident to an aperture, an electric field at observation point far from the aperture is approximately described by the Kirchhoff integral.

$$\vec{E}(\vec{r}) = \frac{e^{ikr}}{2\pi r}\vec{k} \times \int_A \hat{n} \times \vec{E}(\vec{r'}) e^{-i\vec{k}\cdot\vec{r'}} da'$$

where A is the aperture area, r is the distance from the center of aperture located at origin to the observation point, $\hat{n}$ is the normal vector with a direction to the observation point, $\vec{k}$ is the wave vector directed to the observation point. Considering the observation point is located normal to the aperture, the equation can be reduced to

$$\vec{E}_{\text{far}} = \frac{e^{ikr}}{i\lambda r}\int_A \vec{E}_{\text{near}}(\vec{r'})\, da'$$

Thus, a far field at the observation is directly related to the summation of near field on the sample. For the transmission, the amplitudes from a slit array with gap size, d, and a bare reference

are written as

$$E_{\text{sample}} = \frac{e^{ikr}}{i\lambda r}\int_A E_{\text{gap,near}}\, da' = \frac{e^{ikr}}{i\lambda r} E_{\text{gap}} dlN$$

$$E_{\text{ref}} = \frac{e^{ikr}}{i\lambda r}\int_A E_{0,\text{near}}\, da' = \frac{e^{ikr}}{i\lambda r} E_0 A$$

where l is the slit length covering the aperture, and N is the number of slits in the aperture. Then, the transmitted amplitude for slit array, t can be obtained by

$$t = \left|\frac{E_{\text{sample}}}{E_{\text{ref}}}\right| = \left|\frac{E_{\text{gap}}}{E_0}\right| \cdot \beta$$

where $\beta = dlN/A$, called a coverage ratio is a ratio of entire gap areas in transmitted region to the aperture area, simply obtained by the ratio of gap area to the unit cell of the structure. By definition of field enhancement, $Field\ Enhancement$ is given by

$$Field\ Enhancement = \left|\frac{E_{\text{gap}}}{E_0}\right| = {}^{t}/_{\beta}$$

Consequently, in the transmission measurement for slit array in THz-time domain spectroscopy, the field enhancement can be obtained using the transmitted amplitude divided by the coverage ratio.

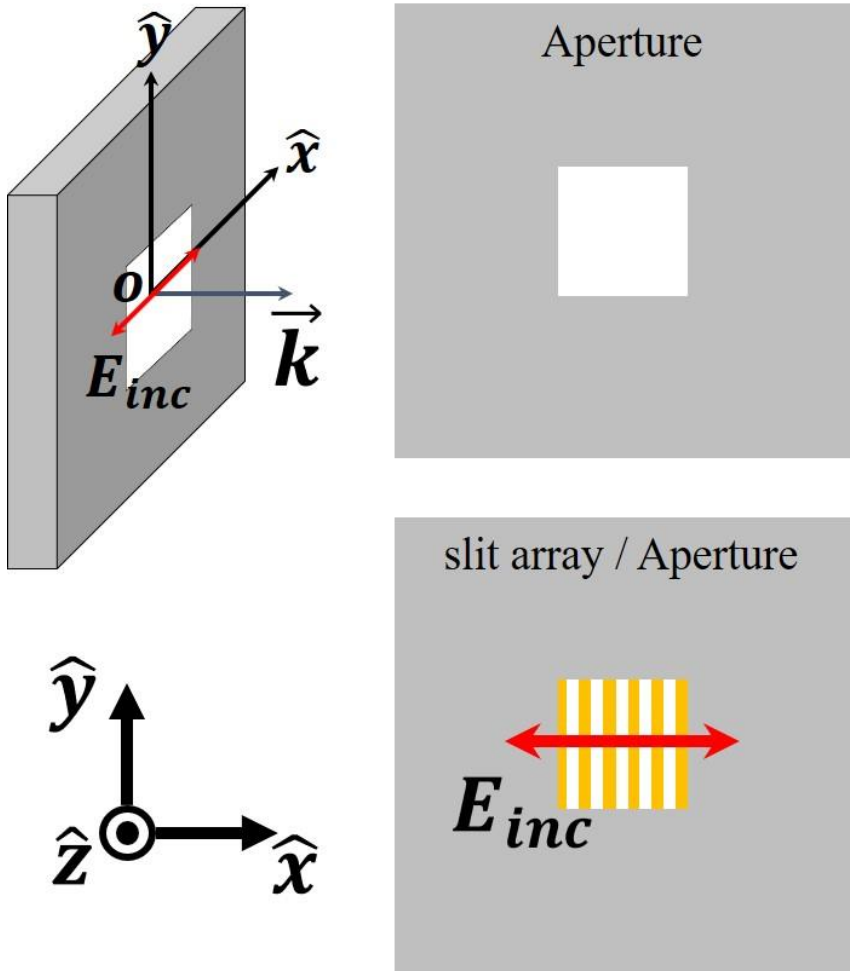

Figure 16. The geometry of experiment for Kirchhoff integral.

Experimental geometry for reference aperture and aperture with slit array sample. When an electric field is incident to the aperture with the horizontal polarization, the diffracted electric field at a point far from the aperture is approximately described by the Kirchhoff integral.

4.3 THz transmission for the graphene gap slit array

The results of THz-time domain spectroscopy for the graphene gap slit array are displayed in Figure 17. An aperture with 2 mm x 2 mm square was used for the Kirchhoff integral formalism. The transmitted THz amplitude through a bare quartz substrate on the aperture in Figure 17(a) was firstly measured as a reference field, E_0, because the graphene gap slit array is on the quartz substrate. The time trace of THz transmitted amplitude for the graphene gap slit array was obtained by subtracting the direct transmission of the Cu thin film, as shown in Figure 17(b). In fact, a transmitted sample field described by Kirchhoff integral precisely includes both the field transmitted through the gaps and directly transmitted field though a metal thin film. The typical direct transmission from a metal film with optically thick can be ignore due to small amplitude. However, the graphene gap slit array shown in Figure 14 has the Cu film with asymmetric thickness, as the film thickness is 400 nm and 50 nm for the 1st Cu film and the 2nd Cu film, respectively. In this asymmetric structure, the effective gap thickness follows the small thickness [64]. In addition, Since the skin depth of a Cu film is about 92 nm at 0.5 THz, Thus, the direct transmission for the graphene gap slit array should be considered for measuring the gap field. From the results of THz measurement, it is found that the graphene gap slit array is fully

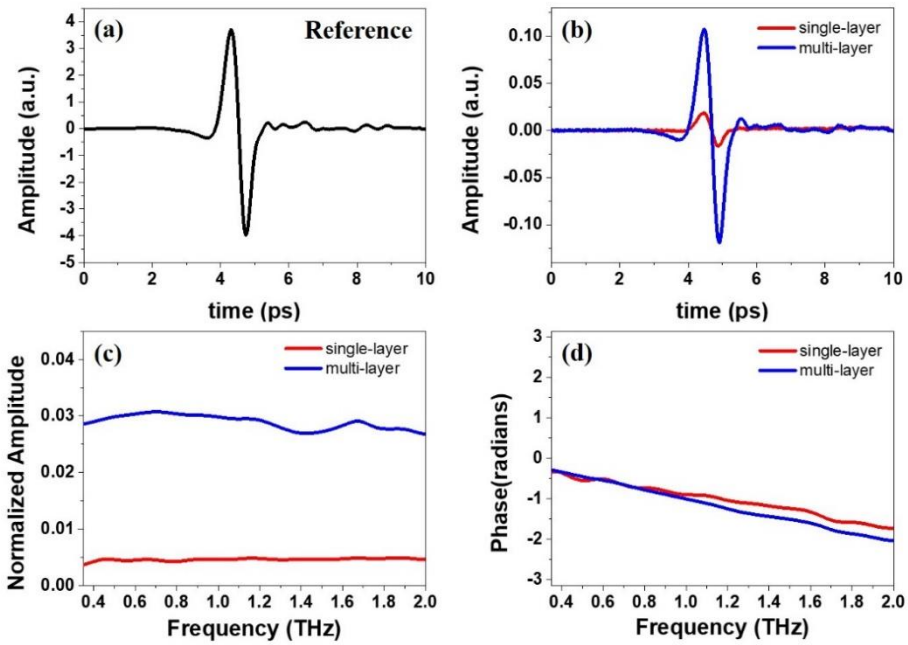

Figure 17. The THz transmitted amplitude through the graphene gap slit array.

(a) Time trace of THz transmitted amplitude through the quartz substrate, as a reference. (b) THz transmitted amplitude through the graphene gap slit array in the time domain, for the single-layer graphene gap (red) and the multi-layer graphene gap (blue). (c-d) In the frequency domain, (c) normalized THz amplitude and (d) phase obtained using the fast Fourier transformation, for single-layer graphene gap (red) and multi-layer graphene gap (blue).

functional in THz regime even though the gap size is a sub-nanometer size for the single-layer graphene gap. An increase in the transmitted THz amplitude with the gap size for the graphene gap slit array is observed, since the gap size of the multi-layer graphene gap is larger than that of the single-layer graphene gap.

Figure 17(c) and 17(d) show the normalized THz field amplitude and phase in the frequency domain using the fast Fourier transformation of the THz field amplitude in the time domain. Unsimilar to the inversely proportional behavior in the THz frequencies for a nanogap slit array with a Al_2O_3 insulating layer, the normalized THz amplitude for the graphene gap slit array has a constant behavior regardless of the THz frequencies and the phase monotonically decreases [65-67]. It implies that the graphene inside the gap is a lossy material for the THz transmission. The THz normalized amplitude in the frequency domain is around 0.5 % and 3 % for the single-layer and multi-layer graphene gap, respectively. However, it should be noted that the transmitted amplitude value for the graphene gap slit array are quite high, considering the THz waves were only passed through the small gap area.

In Figure 18, the field enhancement inside the graphene gap was obtained by the normalized amplitude divided by the coverage ratio, as the calculation (t/β) described in the Kirchhoff integral.

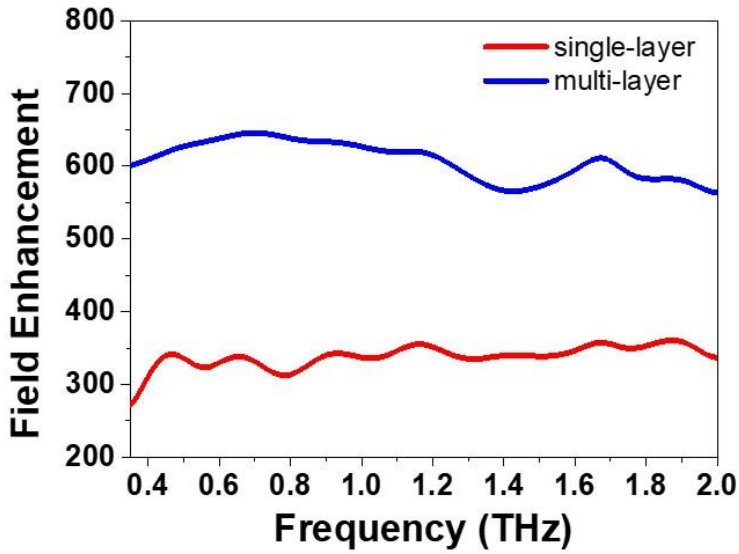

Figure 18. The field enhancement for the graphene gap.

The field enhancement inside the graphene gap obtained by the Kirchhoff integral for the single-layer graphene gap (red) and the multi-layer graphene gap (blue).

Using the 50 μm period of slits and the gap size obtain from the TEM results, the coverage ratio, β, for the single-layer and multi-layer graphene gap is calculated to be approximately 1.34×10^{-5} and 4.76×10^{-5}, respectively. Thus, the field enhancement for the single-layer and the multi-layer graphene gap is obtained around 350 and 600, respectively. It indicates that the field enhancement of the multi-layer graphene gap is greater than that of the single-layer graphene gap. However, it is noted that field enhancement is associated with both normalized transmitted amplitude and a gap size. While the normalized THz amplitude for the multi-layer graphene gap is 6 times larger than that of the single-layer graphene gap, the gap size is reduced about 3.5 times from the multi-layer graphene to the single-layer graphene. It means that an electric field in single-layer graphene gap is more enhanced for the same normalized transmitted amplitude. Therefore, it still can be argued that the field enhancement increases with decreasing the gap size for the graphene gap array.

4.4 Complex dielectric constant of graphene in out-of-plane direction at THz regime

The results of THz-time domain spectroscopy for the graphene slit array reveals that the graphene inside the gap can be treated as a lossy material for the THz transmission. It means that the graphene can interact with the electric field formed inside the gap, as an effective medium with a complex dielectric constant. In order to obtain the complex dielectric constant of the graphene inside the gap, it is necessary to briefly explain the capacitor model in THz transmission for a subwavelength slit, as illustrated in Figure 19. In the capacitor model, the current induced by an incident electric field is given by

$$I = \frac{2E_0 l}{Z_0}$$

where E_0 is the incident electric field, Z_0 is the vacuum impedance and l is the slit length. Since the induced current is a harmonic oscillation, the charges ($I = dQ/dt$) accumulated at the edges of the metal thin films are given by

$$Q = i\frac{I}{\omega} = i\frac{2E_0 l}{\omega Z_0}$$

where ω is the angular frequency. By definition of the capacitance,

$$C = \frac{Q}{V_{\text{gap}}} = \frac{Q}{E_{\text{gap}} d} = i\frac{2E_0 l}{\omega Z_0 E_{\text{gap}} d}$$

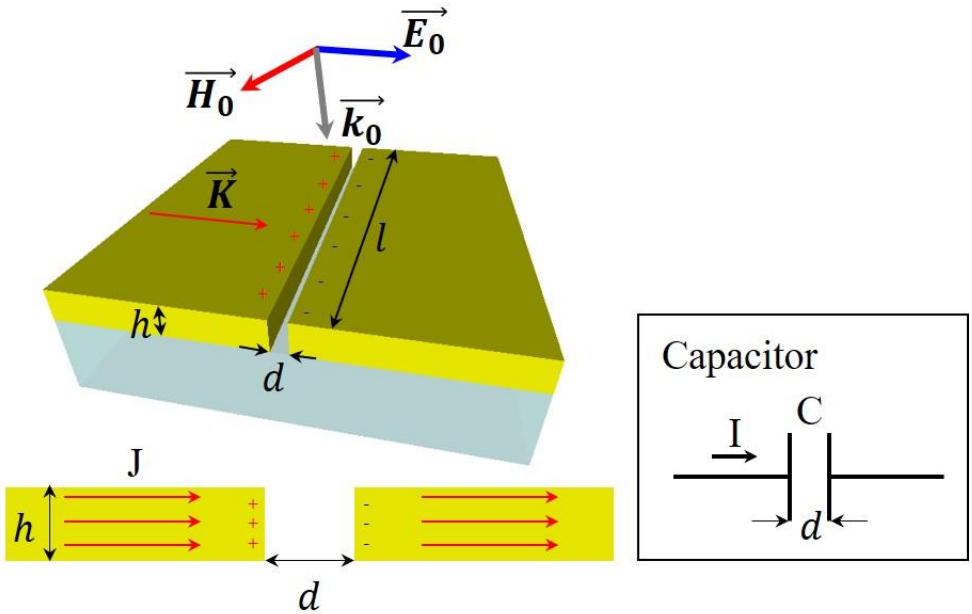

Figure 19. The capacitor model for THz transmission.

The schematic representation of the capacitor model for THz transmission. When a slit with subwavelength gap is illuminated by THz wave with an electric field polarized perpendicular to the slit, the induced currents are generated in the metal thin film. Charges are then accumulated at the edges of the metal thin film, like a capacitor, which results in the large electric fields formed inside the gap.

where V_{gap} is the voltage applied in the gap and d is the gap size. On the other hand, the capacitance in parallel planes is given by

$$C = \varepsilon_0 \varepsilon_{gap} \frac{hl}{d}$$

where ε_0 is the vacuum permittivity, ε_{gap} is the complex dielectric constant of a gap material and h is the thickness of gap. Then, the complex dielectric constant of the gap material is written as

$$\varepsilon_{gap} = i \frac{2E_0}{\omega \varepsilon_0 Z_0 h E_{\mathrm{gap}}}$$

Since the field enhancement is defined as, $Field\ Ehancement = \left| E_{\mathrm{gap}} / E_0 \right|$,

$$\frac{E_{\mathrm{gap}}}{E_0} = Field\ Ehancement \cdot e^{i\varphi}$$

where φ is the phase obtained using the fast Fourier transformation from a THz-time domain spectroscopy measurement. Finally, the complex dielectric constant of a gap material for a slit is written as

$$\therefore \varepsilon_{gap} = \frac{\lambda}{\pi h (Field\ Ehancement)} e^{-i(\varphi - \frac{\pi}{2})}$$

As a result, a complex dielectric constant of a gap material for a subwavelength slit array can be obtained by the capacitor model analysis.

In Figure 20, since the graphene is vertically aligned to the quartz substrate, the out-of-plane complex dielectric constant of graphene in the gap was obtained by the capacitor model using the

results of the THz-time domain spectroscopy for the graphene gap slit array. The values in the THz frequencies for the graphene are reasonable compared to that of graphite previously reported [68]. In Figure 20(a), The real part has negative values for the single-layer and multi-layer graphene both. Furthermore, the single-layer graphene has lower real part than that of the multi-layer graphene. This implies that metallic characteristics of the graphene in the out-of-plane direction similar to the van der Waals gap tunneling in a metal-graphene structure [69]. Due to the tunneling transport, some of charges accumulated at the edges of the Cu thin films can be transferred through the gap, which leads to reduce the field enhancement and THz transmitted amplitude. That is why the graphene gap slit array has the low THz transmittance compared to an Al_2O_3 nanogap slit array with the gap size similar to the multi-layer graphene gap [66, 67]. It is found that the metallicity of the graphene in the out-of-plane direction is reduced with the increase in the number of graphene layers, which implies it is hard for the charges to pass through the gap incrementally. Therefore, the normalized THz amplitude of the single-layer graphene gap is much smaller than that of the multi-layer graphene gap, even though the gap size is 3.5 times reduced.

In Figure 20(b), the imaginary part of the graphene gap shows

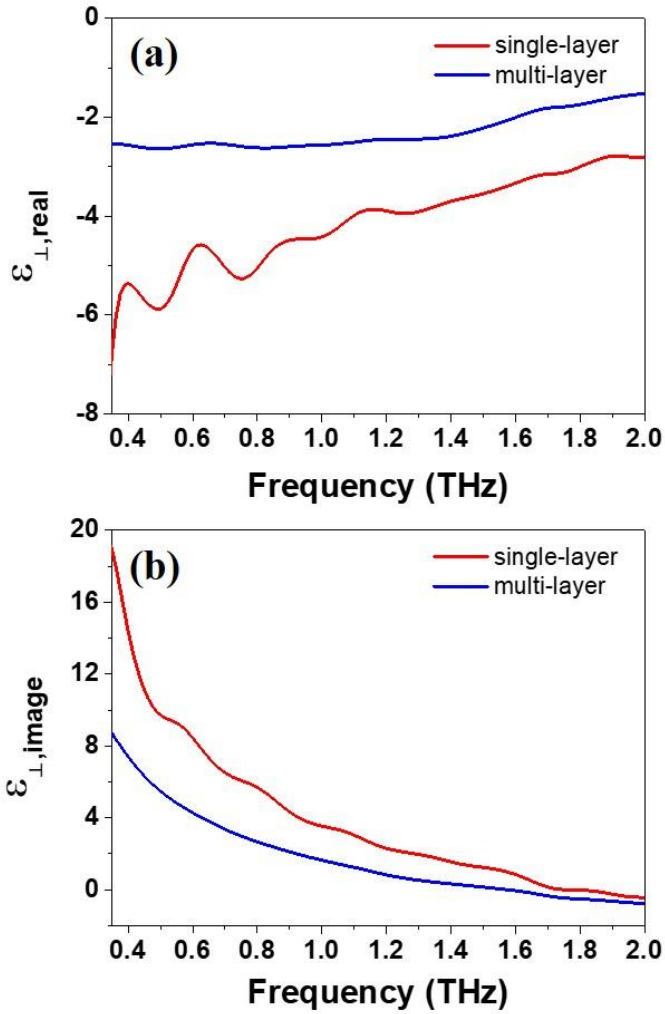

Figure 20. The out-of-plane complex dielectric constant of graphene inside the gap at the THz regime.

(a) the real part and (b) the imaginary part of the out-of-plane complex dielectric constant for the graphene in the gap at THz regime.

the inversely proportional behavior as a function of THz frequency. In order to explain the $1/f$ behavior of imaginary part for the graphene, it is needed to consider the boundary condition, $D_{\mathrm{Cu}} = D_{\mathrm{gap}}$, at the interface between the graphene and the Cu layer in the normal direction. The complex dielectric constant of Cu is mostly imaginary at the THz frequency, $\varepsilon_{\mathrm{Cu}} \approx i\frac{\sigma_{\mathrm{Cu}}}{\varepsilon_0 \omega}$. Eventually, the imaginary part of complex dielectric constant of graphene has the $1/f$ dependency to satisfy the boundary condition, which results in the constant normalized THz amplitude.

The optical properties of the graphene with complex dielectric constant inside the gap at the THz frequencies can effectively demonstrate the results of the THz-time domain spectroscopy measurement. As a result, these results can be provided for the optical conductivity of the graphene in electronic and optical applications. Also, based on the analysis of the capacitor model, optical properties of a sub-nanometer gap array using the other two-dimensional materials such as h-BN, MoS_2, WS_2, etc can be investigated for nanogap-based applications.

Chapter 5. Conclusion

In this thesis, the graphene gap array with a vertical alignment and a sub-nanometer gap size was successfully realized to demonstrate its optical properties at the THz regime. The graphene gap array was prepared by the atomic layer lithography with the PECVD in which the graphene was conformally synthesized on the patterned Cu thin film. In order to fabricate the graphene gap array, two investigations for the graphene synthesis and the Cu surface morphology variation in the PECVD was previously performed before the atomic layer lithography. The results of Raman spectroscopy and AFM measurements suggested the optimal synthesis conditions for the graphene and the Cu thin film in the PECVD. In addition, the structural characterization of the graphene gap array by the SEM and the TEM measurements revealed the achievement of the fabrication for the graphene gap array and the defining the gap size by a multiple of the van der Waals distance according to the number of graphene layers. For the gap size, the graphene gap array can be controlled from the minimum gap size of 0.67 nm to a multiple of the van der Waals distance. The optical properties of the graphene gap slit array at the THz regime was also characterized by the THz-time domain spectroscopy. THz transmitted amplitude through the graphene gap

slit array indicates that the graphene gap slit array is effectively functional at THz regime even though the gap is in a sub-nanometer scale for the single-layer graphene gap. The field enhancement obtained by the analysis of the Kirchhoff integral was around 350 and 600 for the single-layer and multi-layer graphene gap slit array, respectively. Due to the constant normalized THz amplitude for the graphene gap slit array, the graphene was treated as a gap material with a complex dielectric constant interacting with the electric field formed inside the gap. Based on the analysis of the capacitor model, the obtained complex dielectric constant of the graphene in the out-of-plane direction shows that the metallic nature of the graphene and satisfying the boundary condition at interface between the Cu layer and the graphene, which effectively explain the optical properties of the graphene gap slit array at the THz frequencies. The results of this work are expected to open up new way for fabrication techniques, structural and optical properties of other two-dimensional materials, such as h-BN, MoS_2, WS_2, etc. in nanogap-based electronic, optical applications.

Bibliography

[1] T. W. Ebbesen, H. J. Lezec, H. Ghaemi, T. Thio, and P. A. Wolff, "Extraordinary optical transmission through sub-wavelength hole arrays," *Nature,* vol. 391, no. 6668, pp. 667, 1998.

[2] J. Porto, F. Garcia-Vidal, and J. Pendry, "Transmission resonances on metallic gratings with very narrow slits," *Physical review letters,* vol. 83, no. 14, pp. 2845, 1999.

[3] J. Bravo-Abad, F. García-Vidal, and L. Martín-Moreno, "Resonant transmission of light through finite chains of subwavelength holes in a metallic film," *Physical review letters,* vol. 93, no. 22, pp. 227401, 2004.

[4] S. A. Maier, *Plasmonics: fundamentals and applications*: Springer Science & Business Media, 2007.

[5] D. R. Ward, F. Huser, F. Pauly, J. C. Cuevas, and D. Natelson, "Optical rectification and field enhancement in a plasmonic nanogap," *Nat. Nanotechnology,* vol. 5, no. 10, pp. 732-6, Oct, 2010.

[6] W. Kubo, and S. Fujikawa, "Au double nanopillars with nanogap for plasmonic sensor," *Nano Lett.,* vol. 11, no. 1, pp. 8-15, 2010.

[7] J. Lee, M. Seo, D. Park, D. Kim, S. Jeoung, C. Lienau, Q.-H. Park, and P. Planken, "Shape resonance omni-directional terahertz filters with near-unity transmittance," *Optics express,* vol. 14, no. 3, pp. 1253-1259, 2006.

[8] J. Lee, M. Seo, D. Kang, K. Khim, S. Jeoung, and D. Kim, "Terahertz electromagnetic wave transmission through random arrays of single rectangular holes and slits in thin metallic sheets," *Physical review letters,* vol. 99, no. 13, pp. 137401, 2007.

[9] M. Seo, H. Park, S. Koo, D. Park, J. Kang, O. Suwal, S. Choi, P. Planken, G. Park, and N. Park, "Terahertz field enhancement by a metallic nano slit operating beyond the skin-depth limit," *Nature Photonics,* vol. 3, no. 3, pp. 152, 2009.

[10] M. A. Ordal, L. L. Long, R. J. Bell, S. E. Bell, R. R. Bell, R. W. Alexander, and C. A. Ward, "Optical properties of the metals Al, Co, Cu, Au, Fe, Pb, Ni, Pd, Pt, Ag, Ti, and W in the infrared and far infrared," *Applied Optics,* vol. 22, no. 7, pp. 1099-1119, 1983/04/01, 1983.

[11] J.-H. Kang, D. Kim, and Q.-H. Park, "Local capacitor model for plasmonic electric field enhancement," *Physical Review Letters,* vol. 102, no. 9, pp. 093906, 2009.

[12] M. Seo, A. Adam, J. Kang, J. Lee, K. Ahn, Q. H. Park, P. Planken, and D. Kim, "Near field imaging of terahertz focusing onto rectangular apertures," *Optics express,* vol. 16, no. 25, pp. 20484-20489, 2008.

[13] D. Kim, J. Jeong, G. Choi, Y.-M. Bahk, T. Kang, D. Lee, B. Thusa, and D.-S. Kim, "Giant Field Enhancements in Ultrathin Nanoslots above 1 Terahertz," *ACS Photonics,* vol. 5, no. 5, pp. 1885-1890, 2018/05/16, 2018.

[14] H.-R. Park, K. J. Ahn, S. Han, Y.-M. Bahk, N. Park, and D.-S. Kim, "Colossal absorption of molecules inside single terahertz nanoantennas," *Nano letters,* vol. 13, no. 4, pp. 1782-1786, 2013.

[15] D.-K. Lim, K.-S. Jeon, H. M. Kim, J.-M. Nam, and Y. D. Suh, "Nanogap-engineerable Raman-active nanodumbbells for single-molecule detection," *Nature Materials,* vol. 9, no. 1, pp. 60-67, 2010/01/01, 2010.

[16] S. H. M. Jafri, T. Blom, A. Wallner, K. Welch, M. Strømme, H. Ottosson, and K. Leifer, "Control of junction resistances in molecular electronic devices fabricated by FIB," *Microelectronic Engineering,* vol. 88, no. 8, pp. 2629-2631, 2011.

[17] T. Blom, K. Welch, M. Strömme, E. Coronel, and K. Leifer, "Fabrication and characterization of highly reproducible, high resistance nanogaps made by focused ion beam milling," *Nanotechnology,* vol. 18, no. 28, pp. 285301, 2007.

[18] A. Cui, Z. Liu, H. Dong, F. Yang, Y. Zhen, W. Li, J. Li, C. Gu, X. Zhang, and R. Li, "Mass production of nanogap electrodes

toward robust resistive random access memory," *Adv. Mater.,* vol. 28, no. 37, pp. 8227–8233, 2016.

[19] D. J. Beesley, J. Semple, L. K. Jagadamma, A. Amassian, M. A. McLachlan, T. D. Anthopoulos, and J. C. Demello, "Sub–15–nm patterning of asymmetric metal electrodes and devices by adhesion lithography," *Nat. Communications,* vol. 5, pp. 3933, 2014.

[20] S. K. Kim, H. Cho, H.–J. Park, D. Kwon, J. M. Lee, and B. H. Chung, "Nanogap biosensors for electrical and label–free detection of biomolecular interactions," *Nanotechnology,* vol. 20, no. 45, pp. 455502, 2009.

[21] H. Li, I. H. Wani, A. Hayat, S. H. M. Jafri, and K. Leifer, "Fabrication of reproducible sub–5 nm nanogaps by a focused ion beam and observation of Fowler–Nordheim tunneling," *Appl. Phys. Lett.,* vol. 107, no. 10, pp. 103108, 2015.

[22] W. Xu, J. Xiao, Y. Chen, Y. Chen, X. Ling, and J. Zhang, "Graphene-Veiled Gold Substrate for Surface-Enhanced Raman Spectroscopy," *Adv. Mater.,* vol. 25, no. 6, pp. 928–933, 2013.

[23] Q. Xiang, X. Zhu, Y. Chen, and H. Duan, "Surface enhanced Raman scattering of gold nanoparticles supported on copper foil with graphene as a nanometer gap," *Nanotechnology,* vol. 27, no. 7, pp. 075201, 2016.

[24] X. Li, W. C. Choy, X. Ren, D. Zhang, and H. Lu, "Highly intensified surface enhanced Raman scattering by using monolayer graphene as the nanospacer of metal film–metal nanoparticle coupling system," *Adv. Funct. Mater.,* vol. 24, no. 21, pp. 3114–3122, 2014.

[25] A. V. Zaretski, B. C. Marin, H. Moetazedi, T. J. Dill, L. Jibril, C. Kong, A. R. Tao, and D. J. Lipomi, "Using the thickness of graphene to template lateral subnanometer gaps between gold nanostructures," *Nano Lett.,* vol. 15, no. 1, pp. 635–640, 2015.

[26] Z. Zhan, L. Liu, W. Wang, Z. Cao, A. Martinelli, E. Wang, Y. Cao, J. Chen, A. Yurgens, and J. Sun, "Ultrahigh surface-enhanced

Raman scattering of graphene from Au/Graphene/Au sandwiched structures with subnanometer gap," *Adv. Opt. Mater.,* vol. 4, no. 12, pp. 2021–2027, 2016.

[27] J. Mertens, A. L. Eiden, D. O. Sigle, F. Huang, A. Lombardo, Z. Sun, R. S. Sundaram, A. Colli, C. Tserkezis, and J. Aizpurua, "Controlling subnanometer gaps in plasmonic dimers using graphene," *Nano Lett.,* vol. 13, no. 11, pp. 5033–5038, 2013.

[28] A. C. Neto, F. Guinea, N. M. Peres, K. S. Novoselov, and A. K. Geim, "The electronic properties of graphene," *Reviews of modern physics,* vol. 81, no. 1, pp. 109, 2009.

[29] A. Reina, X. Jia, J. Ho, D. Nezich, H. Son, V. Bulovic, M. S. Dresselhaus, and J. Kong, "Large area, few–layer graphene films on arbitrary substrates by chemical vapor deposition," *Nano Lett.,* vol. 9, no. 1, pp. 30–35, 2009.

[30] S. Bae, H. Kim, Y. Lee, X. Xu, J.–S. Park, Y. Zheng, J. Balakrishnan, T. Lei, H. R. Kim, and Y. I. Song, "Roll–to–roll production of 30–inch graphene films for transparent electrodes," *Nat. Nanotechnology,* vol. 5, no. 8, pp. 574, 2010.

[31] X. Li, Y. Zhu, W. Cai, M. Borysiak, B. Han, D. Chen, R. D. Piner, L. Colombo, and R. S. Ruoff, "Transfer of large–area graphene films for high–performance transparent conductive electrodes," *Nano Lett.,* vol. 9, no. 12, pp. 4359–4363, 2009.

[32] Y.–G. Jeong, S. Han, J. Rhie, J.–S. Kyoung, J.–W. Choi, N. Park, S. Hong, B.–J. Kim, H.–T. Kim, and D.–S. Kim, "A vanadium dioxide metamaterial disengaged from insulator–to–metal transition," *Nano letters,* vol. 15, no. 10, pp. 6318–6323, 2015.

[33] H. R. Park, S. Namgung, X. Chen, N. C. Lindquist, V. Giannini, Y. Francescato, S. A. Maier, and S. H. Oh, "Perfect Extinction of Terahertz Waves in Monolayer Graphene over 2-nm-Wide Metallic Apertures," *Adv. Opt. Mater.,* vol. 3, no. 5, pp. 667–673, 2015.

[34] G. Choi, Y.–M. Bahk, T. Kang, Y. Lee, B. H. Son, Y. H. Ahn, M. Seo, and D.–S. Kim, "Terahertz Nanoprobing of Semiconductor Surface Dynamics," *Nano letters,* vol. 17, no.

10, pp. 6397−6401, 2017.

[35] G. Choi, T. Kang, M. Seo, D.−S. Kim, and Y.−M. Bahk, "Enhanced surface carrier response by field overlapping in metal nanopatterned semiconductor," *ACS Photonics,* vol. 5, no. 12, pp. 4739−4744, 2018.

[36] J. Jeong, H. S. Yun, D. Kim, K. S. Lee, H. K. Choi, Z. H. Kim, S. W. Lee, and D. S. Kim, "High Contrast Detection of Water-Filled Terahertz Nanotrenches," *Advanced Optical Materials,* vol. 6, no. 21, pp. 1800582, 2018.

[37] R. P. Chaudhary, B. Das, S. I. Oh, and D.−S. Kim, "Efficient Control of THz Transmission of PEDOT:PSS with Resonant Nano−Metamaterials," *Scientific Reports,* vol. 9, no. 1, pp. 17681, 2019/11/27, 2019.

[38] M. Saito, T. Kano, T. Seki, and M. Miyagi, "Microwire arrays for infrared polarizers," *Infrared physics & technology,* vol. 35, no. 5, pp. 709−714, 1994.

[39] S.−W. Ahn, K.−D. Lee, J.−S. Kim, S. H. Kim, J.−D. Park, S.−H. Lee, and P.−W. Yoon, "Fabrication of a 50 nm half−pitch wire grid polarizer using nanoimprint lithography, " *Nanotechnology,* vol. 16, no. 9, pp. 1874, 2005.

[40] I. Yamada, K. Takano, M. Hangyo, M. Saito, and W. Watanabe, "Terahertz wire−grid polarizers with micrometer−pitch Al gratings," *Optics letters,* vol. 34, no. 3, pp. 274−276, 2009.

[41] W. Park, Y. Lee, T. Kang, J. Jeong, and D.−S. Kim, " Terahertz−driven polymerization of resists in nanoantennas," *Scientific reports,* vol. 8, no. 1, pp. 1−6, 2018.

[42] X. Chen, H.−R. Park, M. Pelton, X. Piao, N. C. Lindquist, H. Im, Y. J. Kim, J. S. Ahn, K. J. Ahn, and N. Park, "Atomic layer lithography of wafer−scale nanogap arrays for extreme confinement of electromagnetic waves, " *Nature communications,* vol. 4, no. 1, pp. 1−7, 2013.

[43] J. Rhie, D. Lee, Y.−M. Bahk, J. Jeong, G. Choi, Y. Lee, S. Kim, S. Hong, and D.−S. Kim, "Control of optical nanometer gap shapes made via standard lithography using atomic layer

deposition," *Journal of Micro/Nanolithography, MEMS, and MOEMS,* vol. 17, no. 2, pp. 023504, 2018.

[44] S. M. George, "Atomic layer deposition: an overview," *Chemical reviews,* vol. 110, no. 1, pp. 111-131, 2010.

[45] X. Li, W. Cai, J. An, S. Kim, J. Nah, D. Yang, R. Piner, A. Velamakanni, I. Jung, and E. Tutuc, "Large-area synthesis of high-quality and uniform graphene films on copper foils," *Science,* vol. 324, no. 5932, pp. 1312-1314, 2009.

[46] X. Li, W. Cai, L. Colombo, and R. S. Ruoff, "Evolution of graphene growth on Ni and Cu by carbon isotope labeling," *Nano Lett.,* vol. 9, no. 12, pp. 4268-4272, 2009.

[47] S. Bhaviripudi, X. Jia, M. S. Dresselhaus, and J. Kong, "Role of kinetic factors in chemical vapor deposition synthesis of uniform large area graphene using copper catalyst," *Nano Lett.,* vol. 10, no. 10, pp. 4128-4133, 2010.

[48] N. Woehrl, O. Ochedowski, S. Gottlieb, K. Shibasaki, and S. Schulz, "Plasma-enhanced chemical vapor deposition of graphene on copper substrates," *AIP Advances,* vol. 4, no. 4, pp. 047128, 2014.

[49] T.-o. Terasawa, and K. Saiki, "Growth of graphene on Cu by plasma enhanced chemical vapor deposition," *Carbon,* vol. 50, no. 3, pp. 869-874, 2012.

[50] M. Abdullah, S. Khairunnisa, and F. Akbar, "Zipper model for the melting of thin films," *Eur. J. Phys.,* vol. 37, no. 1, pp. 015501, 2015.

[51] S. Jin, M. Huang, Y. Kwon, L. Zhang, B. W. Li, S. Oh, J. Dong, D. Luo, M. Biswal, B. V. Cunning, P. V. Bakharev, I. Moon, W. J. Yoo, D. C. Camacho-Mojica, Y. J. Kim, S. H. Lee, B. Wang, W. K. Seong, M. Saxena, F. Ding, H. J. Shin, and R. S. Ruoff, "Colossal grain growth yields single-crystal metal foils by contact-free annealing," *Science,* vol. 362, no. 6418, pp. 1021-1025, Nov 30, 2018.

[52] B. Huet, and J.-P. Raskin, "Role of Cu foil in-situ annealing in controlling the size and thickness of CVD graphene domains,"

Carbon, vol. 129, pp. 270–280, 2018.

[53] Z. Ni, H. Wang, J. Kasim, H. Fan, T. Yu, Y. H. Wu, Y. Feng, and Z. Shen, "Graphene thickness determination using reflection and contrast spectroscopy," *Nano letters,* vol. 7, no. 9, pp. 2758–2763, 2007.

[54] L. Malard, M. Pimenta, G. Dresselhaus, and M. Dresselhaus, "Raman spectroscopy in graphene," *Phys. Rep.,* vol. 473, no. 5–6, pp. 51–87, 2009.

[55] A. C. Ferrari, J. Meyer, V. Scardaci, C. Casiraghi, M. Lazzeri, F. Mauri, S. Piscanec, D. Jiang, K. Novoselov, and S. Roth, "Raman spectrum of graphene and graphene layers," *Phys. Rev. Lett.,* vol. 97, no. 18, pp. 187401, 2006.

[56] A. C. Ferrari, "Raman spectroscopy of graphene and graphite: disorder, electron–phonon coupling, doping and nonadiabatic effects," *Solid state communications,* vol. 143, no. 1–2, pp. 47–57, 2007.

[57] L. Cançado, K. Takai, T. Enoki, M. Endo, Y. Kim, H. Mizusaki, A. Jorio, L. Coelho, R. Magalhaes–Paniago, and M. Pimenta, "General equation for the determination of the crystallite size L a of nanographite by Raman spectroscopy," *Appl. Phys. Lett.,* vol. 88, no. 16, pp. 163106, 2006.

[58] W. Liu, H. Li, C. Xu, Y. Khatami, and K. Banerjee, "Synthesis of high–quality monolayer and bilayer graphene on copper using chemical vapor deposition," *Carbon,* vol. 49, no. 13, pp. 4122–4130, 2011.

[59] J. Cho, L. Gao, J. Tian, H. Cao, W. Wu, Q. Yu, E. N. Yitamben, B. Fisher, J. R. Guest, and Y. P. Chen, "Atomic–scale investigation of graphene grown on Cu foil and the effects of thermal annealing," *ACS nano,* vol. 5, no. 5, pp. 3607–3613, 2011.

[60] I. Calizo, W. Bao, F. Miao, C. N. Lau, and A. A. Balandin, "The effect of substrates on the Raman spectrum of graphene: Graphene– on–sapphire and graphene–on–glass," *Applied Physics Letters,* vol. 91, no. 20, pp. 201904, 2007.

[61] C. Liu, Y. Ma, W. Li, and L. Dai, "The evolution of Raman spectrum of graphene with the thickness of SiO2 capping layer on Si substrate," *Applied Physics Letters,* vol. 103, no. 21, pp. 213103, 2013.

[62] Z. Shen, J. Li, M. Yi, X. Zhang, and S. Ma, "Preparation of graphene by jet cavitation," *Nanotechnology,* vol. 22, no. 36, pp. 365306, 2011.

[63] J. Kyoung, M. Seo, H. Park, K. Ahn, and D. Kim, "Far field detection of terahertz near field enhancement of sub-wavelength slits using Kirchhoff integral formalism," *Optics Communications,* vol. 283, no. 24, pp. 4907-4910, 2010.

[64] S. Han, Y.-M. Bahk, N. Park, and D.-S. Kim, "Terahertz field enhancement in asymmetric and tapered nano-gaps," *Optics express,* vol. 24, no. 3, pp. 2065-2071, 2016.

[65] J. Jeong, J. Rhie, W. Jeon, C. S. Hwang, and D.-S. Kim, "High-throughput fabrication of infinitely long 10 nm slit arrays for terahertz applications," *Journal of Infrared, Millimeter, and Terahertz Waves,* vol. 36, no. 3, pp. 262-268, 2015.

[66] Y.-M. Bahk, S. Han, J. Rhie, J. Park, H. Jeon, N. Park, and D.-S. Kim, "Ultimate terahertz field enhancement of single nanoslits," *Physical Review B,* vol. 95, no. 7, pp. 075424, 2017.

[67] O. K. Suwal, J. Rhie, N. Kim, and D.-S. Kim, "Nonresonant 10 4 Terahertz Field Enhancement with 5-nm Slits," *Sci. Rep.,* vol. 7, pp. 45638, 2017.

[68] L. G. Johnson, and G. Dresselhaus, "Optical properies of graphite," *Phys. Rev. B,* vol. 7, no. 6, pp. 2275, 1973.

[69] X. Zhu, S. Lei, S.-H. Tsai, X. Zhang, J. Liu, G. Yin, M. Tang, C. M. Torres Jr, A. Navabi, and Z. Jin, "A study of vertical transport through graphene toward control of quantum tunneling," *Nano letters,* vol. 18, no. 2, pp. 682-688, 2018.

국문초록

수직으로 정렬된 그래핀 갭의 제작과 테라헤르츠파 영역에서의 특성

김성환
물리천문학부 물리학전공
서울대학교

본 연구는 구리-그래핀-구리 구조로 수직으로 정렬된 그래핀 갭의 테라헤르츠파 영역에서 광학적 특성을 알아보기 위해 진행되었다. 그래핀 갭을 갖는 슬릿 배열은 패턴 된 구리 박막 상에 그래핀을 직접 합성한 후, 그 위에 두 번째 구리층을 증착함으로써 제조되었다. 구리 표면에서 합성된 그래핀의 구조적 특징은 구면 수차 보정 투과 전자 현미경 및 공명 라만 분광학에 의해 특성화되었다. 결과는 플라즈마 강화 화학 기상 증착 공정에서 합성 온도 및 사전 열처리 시간을 조정함으로써 구리 표면상의 그래핀의 층 수 및 결정도를 제어할 수 있음을 밝혀냈다. 또한, 그래핀 갭의 크기는 그리팬 층의 수에 따른 반 데르 발스 거리의 배수에 의해 정해질 수 있음을 확인하였다. 테라헤르츠파 영역에서 그래핀 갭 슬릿 배열의 광학적 특성을 조사하기 위해 테라 헤르츠-시간 영역 분광학을 수행하였다. 갭 크기가 단층 그래핀갭에 대해 서브-나노미터임에도 불구하고, 테라헤르츠파 투과 진폭은 제조된 그래핀 갭 슬릿 배열이 테라헤르츠파 영역에서 완전히 작동하는 것을 보여주었다. 테라

헤르츠파의 일정한 투과 진폭은 축전기 모델을 이용하여 갭 안에 그래핀을 복소 유전 상수를 갖는 갭 물질로 하여 분석되었다. 이 연구 결과는 육방 정계 질화 붕소 (h-BN), 이황화 몰리브덴 (MoS_2) 등과 같은 2 차원 물질을 사용하여 광학, 전자 및 광전자 응용 분야에서 구조 제작 기술 및 구조적, 광학적 특성화를 위한 새로운 방법을 제시할 것으로 기대된다.

Keywords : 나노갭, 그래핀, 원자층 리소그래피, 라만 분광학, 테라헤르츠 시간영역분광학

Student Number : 2013-30918